

Article

Overall Adaptive Controller Design of PMSG Under Whole Wind Speed Range: A Perturbation Compensation Based Approach

Jian Chen ¹, Wenyong Duan ¹, Xiaodong Yang ¹, Lanhong Zhang ¹, Yi Shan ², Bo Yang ^{3,*}, Hongchun Shu ³, Na An ³ and Tao Yu ⁴ 

¹ School of Electrical Engineering, Yancheng Institute of Technology, Yancheng 224051, China; cjycit@163.com (J.C.); dwy1985@126.com (W.D.); cumtyxd@126.com (X.Y.); zlhycit@126.com (L.Z.)

² Jiangsu Jinfeng Technology Co., Ltd., Yancheng 224199, China; shanyi@goldwind.com.cn

³ Faculty of Electric Power Engineering, Kunming University of Science and Technology, Kunming 650500, China; yangboffg@sina.com (H.S.); Anna073000@163.com (N.A.)

⁴ College of Electric Power, South China University of Technology, Guangzhou 510640, China; taoyu1@scut.edu.cn

* Correspondence: yangbo_ac@outlook.com; Tel.: +86-183-1459-6103

Received: 18 September 2019; Accepted: 9 October 2019; Published: 12 October 2019



Abstract: This paper proposes an adaptive overall control strategy of the permanent magnet synchronous generator-based wind energy conversion system (WECS) in the whole wind speed range. For the machine side, the maximum power point tracking (MPPT) operation is realized by stator current and mechanical rotation speed control under below-rated wind speeds. Under above-rated wind speeds, the extracted wind power is limited via pitch control. For the grid side, the reactive and active power injected into grid is regulated by DC-Link voltage and grid current control loop. In addition, under grid voltage dips, the pitch control is employed for limiting grid current and maintaining the DC-Link voltage around its rated value. The fault ride-through capability (FRTC) can be enhanced. The overall control strategy is based on perturbation estimation technique. A designed observer is used for estimating the perturbation term including all system nonlinearities, uncertainties and disturbances, so as to compensate the real perturbation. Then, an adaptive control for the original nonlinear system can be realized. The effectiveness of the proposed overall control strategy is verified by applying the strategy to a 2-MW WECS in MATLAB/Simulink. The results show that, compared with the feedback linearizing control (FLC) strategy and conventional vector control (VC) strategy, the proposed perturbation observer based adaptive control (PO-AC) strategy realizes the control objectives without knowing full state information and accurate system model, and improves the robustness of the WECS parameter uncertainties and FRTC.

Keywords: wind energy conversion system (WECS); overall adaptive control strategy; limit extracted power; maximum power point (MPPT); fault ride-through capability (FRTC)

1. Introduction

Recent years, renewable energy sources have attracted a lot attention, in which wind energy is the fastest growing and most competitive source so far, because it is clean, safe and exhaustless [1–3]. Recently, the world market share of wind energy conversion systems (WECSs) is dominated by the variable-speed wind turbines (VSWTs) due to their merits, e.g., high power quality and efficiency [4,5]. Moreover, the VSWTs can control output power and wind turbine (WT) speed for the reduction of stresses and load on blades and tower. Nowadays, doubly fed induction generators (DFIGs) based VSWTs occupy a large market share of the WECSs with the advantages such as large operation

region, small capability of power electronic devices and full decoupled control of reactive and active power [6,7]. However, a gearbox is required for coupling the generator to the WT in the WECS based on DFIG, which increases failure rate and maintenance expenses [8–10]. Recently, permanent magnet synchronous generators (PMSGs) based WECSs are without gearboxes, and possess merits e.g., self-excitation, fast dynamic response, low noise, and high efficiency [11–17]. Usually, an AC-DC-AC converter system connects a PMSG to the power grid in the WECS, which is shown in Figure 1.

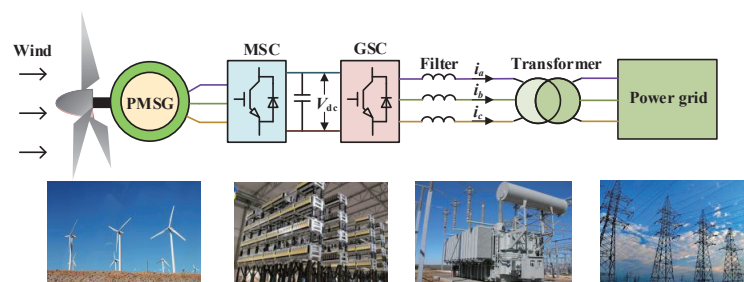


Figure 1. Configuration of a PMSG-WT based WECS.

In the WECS, it consists two voltage-source converters (VSCs), i.e., a grid-side converter (GSC) and a machine-side converter (MSC). The GSC is responsible for maintaining the DC-Link voltage and delivering active power to the grid, whereas the objective of the MSC is controlling generating power of the generator. The well regulated DC-Link voltage can decouple the control of the GSC and MSC. In addition, for the control of the MSC, the maximum wind power can be extracted through using speed control or torque control under below-rated wind speeds [18–21]. Meanwhile pitch control methods have been proposed to limit the extracted wind power under above-rated wind speeds [22–24]. However, the works of control strategies based on whole wind speed range for WTs are relatively few. In this paper, an overall control strategy for the WECS in the whole wind speed range including mechanical rotation speed control at below-rated speeds and pitch control at rated power area, and the GSC control, has been considered.

In addition, the grid integration of the WECSs has been enforced more and more regulations with sharp increment of wind energy penetrating into the grid [25–29]. According to the requirements of the grid codes, the wind farms should provide fault ride-through capability (FRTC) during or after grid faults. To meet these requirements, the WECSs are required to remain connected to the grid during grid faults, and supply the generating power to the grid when the grid faults are cleared. A stable operation is important for the grid and WECS. Additional protection devices, e.g., active crowbars and damping resistor, have been installed in PMSG and DFIG based WECSs for enhancing the FRTC of WECSs [30–33]. Although the FRTC of the WECSs has been enhanced, the cost of the whole system has been increased by installing the additional protection devices. Another effective way of enhancing the FRTC of WECSs is improving or redesigning the control algorithms of the VSCs. It can avoid installing extra equipment, and the power rating of the protection devices can be reduced [34–40]. Numerous designed controllers have been studied for the control of the GSC, i.e., feedback linearisation control (FLC), conventional vector control with proportional-integral (VC) loops, sliding mode control, and perturbation observer based adaptive control (PO-AC) [40–46]. Although these advanced control methods have provided satisfactory performances of the GSC and enhanced the FRTC of the WECSs based on the PMSGs, all these works assumed that a current source can simply replace the generator output. The reduction of generator output is simultaneous and proportional to the decrement of the grid voltage. In addition, the dynamics of the machine-side during the tests of different voltage dips have not been considered in [39–41] or have been simply simulated by varying current in [45]. However, a real WT cannot be simply replaced by a current source. In this paper, a pitch control strategy is employed for assisting the WECS operation under grid voltage dips. Without additional

devices, the pitch control strategy can be applied in reducing the extracted wind power by changing pitch angle once grid voltage dips is detected.

To investigate the performances of the permanent magnet synchronous generator based wind turbine (PMSG-WT) under normal and fault operation conditions, an overall adaptive control approach for the WECS has been proposed. This paper integrates the author's previous works reported in [45,47]. Under normal operation condition, for MSC control, the maximum power point tracking (MPPT) operation is realized by mechanical rotation speed control and stator current control under below-rated wind speeds. The proposed MPPT control method in [47] is employed in this paper. It requires mechanical rotation speed to track its optimal value. Under above-rated wind speeds, the extracted wind power is limited by mechanical rotation speed control and stator current control. The mechanical rotation speed and stator currents are required to track their rated values, respectively. For GSC control, the reactive and active power injected into grid is regulated by using grid current control and DC-Link voltage control loop designed in [45]. Under the grid voltage dips, the GSC control strategy adopts the same control strategy as that in normal operation. For the MSC control strategy, only pitch control strategy is applied. The pitch control is employed to assist in enhancing the FRTC of the WECS. The extracted wind power can be reduced through increasing pitch angle. The proposed control strategy provides satisfactory performances in the different operation conditions, e.g., ramp wind speeds and random wind speeds, and enhances the FRTC of the WECS during grid voltage dips.

The remaining parts of this paper is organized as follows. The model of the WECS based on PMSG is presented in Section 2. Section 3 presents the design of the overall PO-AC. In Section 4, simulation studies are carried out for verifying the effectiveness of the proposed PO-AC in comparing with the FLC and VC. Finally, conclusions of this work are presented in Section 5.

2. System Model

The WECS considered in this paper is shown in Figure 1. This section presents the models of the machine and grid sides.

2.1. Model of Machine Side

For the machine side, the state-space model of the PMSG-WT is given as [48]:

$$\dot{x} = f(x) + b_1(x)u_1 + b_2(x)u_2 + b_3(x)u_3 \quad (1)$$

where

$$f(x) = \begin{bmatrix} f_1(x) \\ f_2(x) \\ f_3(x) \\ f_4(x) \end{bmatrix} = \begin{bmatrix} -\frac{\beta}{\tau_\beta} \\ -\frac{R_s}{L_{md}}i_{md} + \frac{\omega_e L_{mq}}{L_{md}}i_{mq} \\ -\frac{R_s}{L_{mq}}i_{mq} - \frac{1}{L_{mq}}\omega_e(L_{md}i_{md} + K_e) \\ \frac{1}{J_{tot}}(T_e - T_m) \end{bmatrix},$$

$$b_1(x) = \left[-\frac{\beta}{\tau_\beta} \quad 0 \quad 0 \quad 0\right]^T,$$

$$b_2(x) = \left[0 \quad \frac{1}{L_{md}} \quad 0 \quad 0\right]^T,$$

$$b_3(x) = \left[0 \quad 0 \quad \frac{1}{L_{mq}} \quad 0\right]^T,$$

$$x = [x_1, x_2, x_3, x_4]^T = [\beta \quad i_{md} \quad i_{mq} \quad \omega_m]^T,$$

$$u = [u_1, u_2, u_3]^T = [\beta_r, V_{md}, V_{mq}]^T,$$

$$y = [y_1, y_2, y_3]^T = [h_1(x), h_2(x), h_3(x)]^T = [\omega_m, i_{md}, i_{mq}]^T$$

where $x \in R^4$, $u \in R^3$ and $y \in R^3$ are state vector, input vector and output vector, respectively; $f(x)$, $b(x)$ and $h(x)$ are smooth vector fields. β and β_r are pitch angle and pitch angle reference, τ_β is the actuator time constant, V_{md} and V_{mq} are the d, q axis stator voltages, i_{md} and i_{mq} are the d, q axis stator currents, L_{md} and L_{mq} are d, q axis stator inductances, R_s is the stator resistance, p is the number of pole pairs, K_e is the field flux given by the magnet, J_{tot} is the total inertia of the drive train, ω_m and

$\omega_e (= p\omega_m)$ are the mechanical and electrical rotation speed, respectively, and T_e and T_m are the WT electromagnetic and mechanical torque, respectively.

The electromagnetic torque is expressed as:

$$T_e = p[(L_{md} - L_{mq})i_{md}i_{mq} + i_{mq}K_e] \quad (2)$$

Under below-rated wind speed, its aim is extracting the maximum wind power, which requires that the maximum power coefficient C_{pmax} should be achieved under time-varying wind speeds. To maintain C_p at its maximum value C_{pmax} , the tip speed ratio λ is required to keep at its optimal value λ_{opt} with a fixed pitch angle β .

$$C_{pmax} = C_p(\lambda_{opt}) \quad (3)$$

To obtain the optimal value of tip speed ratio λ_{opt} , the mechanical rotation speed ω_m is required to track its optimal reference ω_m^* as

$$\omega_m^* = \frac{V}{R}\lambda_{opt} \quad (4)$$

Under above-rated wind speeds, to maintain the extracted wind power at rated power in normal operation, it requires the corresponding pitch angle should be achieved, which in turn requires both the mechanical rotation speed ω_m and the mechanical torque T_m should be kept at their rated values, respectively. The rated mechanical torque T_m is achieved when the electromagnetic torque T_e can track its rated reference T_{er} and the ω_m is kept at its rated value. From (2), it can be seen that the electromagnetic torque T_e can be maintained at T_{er} if the q-axis stator current i_{mq} can track its rated reference i_{mq}^* and i_{md} is kept at 0.

Note that, under the grid voltage dips, the pitch control is employed to reduce the extracted wind power for maintaining the DC-Link voltage V_{dc} at its rated value.

2.2. Model of Grid Side

The state-space model of the GSC of the WECS is expressed as [39]

$$\dot{x} = f(x) + b_4(x)u_4 + b_5(x)u_5 \quad (5)$$

where

$$\begin{aligned} f(x) &= \begin{bmatrix} f_5(x) \\ f_6(x) \\ f_7(x) \end{bmatrix} = \begin{bmatrix} \frac{1}{L_g}E_{gd} - \frac{R_g}{L_g}i_{gd} + \omega i_{gq} \\ \frac{1}{L_g}E_{gq} - \frac{R_g}{L_g}i_{gq} - \omega i_{gd} \\ \frac{3E_{gd}i_{gd}}{2CV_{dc}} - \frac{i_{dc2}}{C} \end{bmatrix}, \\ b_4(x) &= \begin{bmatrix} -\frac{1}{L_g} & 0 & 0 \end{bmatrix}^T, \\ b_5(x) &= \begin{bmatrix} 0 & -\frac{1}{L_g} & 0 \end{bmatrix}^T, \\ x &= [x_5, x_6, x_7]^T = [i_{gd} \quad i_{gq} \quad V_{dc}]^T, \\ u &= [u_4, u_5]^T = [V_{gd}, V_{gq}]^T, \\ y &= [y_4, y_5]^T = [h_4(x), h_5(x)]^T = [i_{gq}, V_{dc}]^T \end{aligned}$$

where $x \in R^3$, $y \in R^2$ and $u \in R^2$ are state, output and input vectors, respectively; $f(x)$, $b(x)$ and $h(x)$ are smooth vector fields. $i_{gd,q}$ are the grid current in the d, q axis, $E_{gd,q}$ are the grid voltage in the d, q axis, $V_{gd,q}$ are the GSC voltage in the d, q axis, L_g and R_g are equivalent inductance and resistance between the high voltage terminals of the grid-connected transformer and GSC, C is capacitance of DC-Link and ω is grid voltage's angular speed, $i_{dc1,2}$ are the grid-side and machine-side DC-Link current, respectively, i_{dc} is the current of the DC-Link capacitor, and V_{dc} is the voltage of the DC-Link capacitor.

When the WECSs encounter the grid voltage dips without protection measures, the DC-Link voltage cannot well regulated. It will result in the sharp increment of the grid-side current, which may

exceed its safe boundary. For the power grid, the varying power injected into the power grid can be seen as disturbance. The objective of the GSC is to enhance the FRTC of the WECS and decouple the control of reactive and active power injected into the power grid.

3. Adaptive Overall Control Approach of the WECS

The brief control block diagram for the proposed control approach of the WECS is shown in Figure 2. For the GSC, the adaptive control approach proposed in author’s previous work [45] has been employed for maintaining the DC-Link voltage at its rated value. For the MSC, under below-rated wind speeds, its objective is capturing maximum wind power. The proposed adaptive control approach has been proposed in author’s previous work [47]. Under above-rated wind speeds, its aim is to limit the extracted wind power through adaptive pitch control. In addition, the adaptive pitch control is employed for limiting extracted wind power under grid voltage dips. The adaptive pitch control is introduced firstly. Then, the control strategy of the WECS operating under normal operation and grid voltage dips will be introduced.

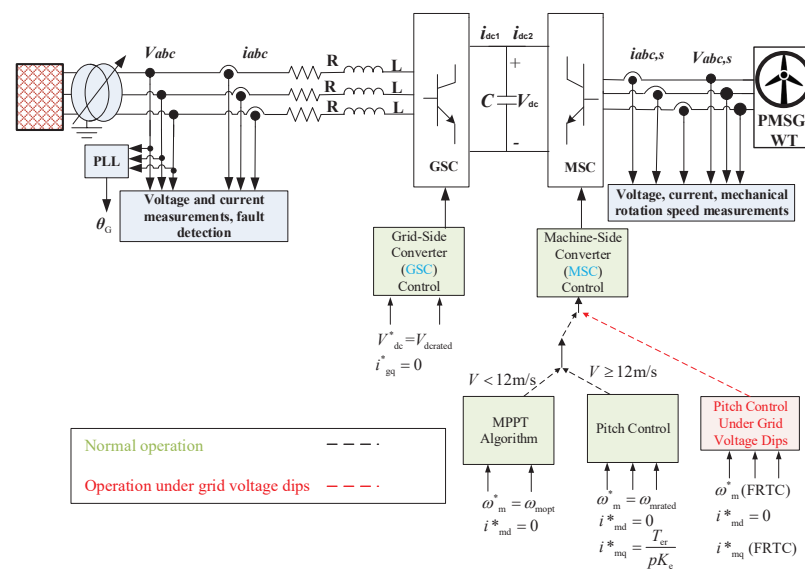


Figure 2. Control block diagram under normal operation and grid voltage dips.

3.1. Adaptive Pitch Control

3.1.1. Design for Proposed Strategy

This section presents the design of the perturbation observer-based PO-AC. For each subsystem in the PMSG-WT, a lumped perturbation term is defined to contain disturbances, subsystem nonlinearities, and interactions between subsystems. Observers are employed for estimating each subsystem state and perturbation term. The estimation processes are implemented via introducing fictitious states. The proposed adaptive control design is illustrated in the following subsections.

3.1.2. States and Perturbation Observer

A canonical control form of studied system is considered as follows

$$\begin{cases} \dot{x}_1 &= x_2 \\ &\vdots \\ \dot{x}_n &= f(x) + b(x)u \\ y &= x_1 \end{cases} \quad (6)$$

and a fictitious state is defined to express the system perturbation, i.e., $x_{n+1} = \Psi$, thus the state equation becomes

$$\begin{cases} \dot{x}_1 &= x_2 \\ &\vdots \\ \dot{x}_n &= x_{n+1} + b(0)u \\ \dot{x}_{n+1} &= \Psi(\cdot) \\ y &= x_1 \end{cases} \quad (7)$$

where $\Psi = f(x) + [b(x) - b(0)]u$, $b(0)$ is the nominal value of $b(x)$. In the system (7), these assumptions are made as follows [49,50].

- A.1. $b(0)$ is chosen to meet: $|b(x)/b(0) - 1| \leq \theta < 1$, where θ is a positive constant.
 A.2. The function $\Psi(x, u, t) : R^n \times R \times R^+ \rightarrow R$ and $\dot{\Psi}(x, u, t) : R^n \times R \times R^+ \rightarrow R$ are locally Lipschitz in their arguments in the domain of interest and are globally bounded in x :

$$|\Psi(x, u, t)| \leq \gamma_1, \quad |\dot{\Psi}(x, u, t)| \leq \gamma_2 \quad (8)$$

where γ_1 and γ_2 are positive constants. Besides, $\Psi(0, 0, 0) = 0$ and $\dot{\Psi}(0, 0, 0) = 0$. Assumption A.2 can assure that the origin is an equilibrium point in the open-loop system.

The perturbations can be estimated by employing the high-gain observer proposed in [49]. $b(x)$ and $f(x)$ are unknown continuous functions under the assumptions A.1 and A.2. State $x_1 = y$ is assumed to be available. Therefore, a $(n+1)$ th-order high-gain observer can be designed as

$$\begin{cases} \dot{\hat{x}}_1 &= \hat{x}_2 + h_1(y - \hat{x}_1) \\ &\dots \\ \dot{\hat{x}}_n &= \hat{x}_{n+1} + h_n(y - \hat{x}_1) + b(0)u \\ \dot{\hat{x}}_{n+1} &= h_{n+1}(y - \hat{x}_1), \end{cases} \quad (9)$$

where $\hat{x}_k, k = 1, 2, \dots, n+1$ are the estimations of $x_k, k = 1, 2, \dots, n+1$, respectively, and $h_{ij} = \alpha_{ij}/\epsilon^i$, $i = 1, 2, 3; j = 1, \dots, r_i + 1$ are the observer gains, $0 < \epsilon \ll 1$ is a specified positive constant and parameters α_{ij} are chosen so that the roots of

$$s^{n+1} + \alpha_{i1}s^n + \dots + \alpha_{ir_i}s + \alpha_{i(r_i+1)} = 0 \quad (10)$$

are in the open left-half complex plan.

3.1.3. Adaptive Control for PMSG-WT

The proposed adaptive control adopts perturbation estimation term $\Psi(\cdot)$ for the compensations of the actual system perturbation and the adaptive feedback linearizing control can be achieved. The detail system model and accurate system parameters are required in conventional FLC design. More details can be found in previous work [45,47,49]. The estimation of x is denoted as \hat{x} in this paper.

For the WT, the objective system output is selected as $y_{WT} = y_1 = \omega_m$, and ω_m^* is the reference value of mechanical rotation speed ω_m . According to Equation (7), differentiate y_1 until the control input appears explicitly, it yields

$$\ddot{y}_1 = \Psi_1 + b1(0)u_1 \quad (11)$$

where $b1(0)$ is nominal value of $b1(x) = \frac{AE\beta}{\tau\beta} [-0.088e^{-12.5\tau} - \frac{0.08V^2}{F} + \frac{0.105\beta^2}{(1+\beta^3)^2}]$, and $A = \frac{\rho\pi R^2 V^3}{2\omega_m}$, $E = (39.27 - 319\tau + 1.1\beta)e^{-12.5\tau}$, $F = \omega_m R + 0.08\beta V$, and $\tau = \frac{1}{\lambda + 0.08\beta} - \frac{0.035}{\beta^3 + 1}$.

According to Equations (6) and (7), the perturbation yields as follows

$$\Psi_1(x) = (b1(x) - b1(0))u_1 + A\left[-\frac{C_p}{\omega_m} - \frac{RV}{F^2}E\right]\frac{d\omega_m}{dt} - \frac{AE\beta}{\tau_\beta}\left[-0.088e^{-12.5\tau} - \frac{0.08V^2}{F} + \frac{0.105\beta^2}{(1+\beta^3)^2}\right]\frac{d\beta}{dt}$$

According Equation (9), a third-order states and perturbation observer (SPO) proposed in [49] is employed for estimating Ψ_1 as

$$\begin{cases} \dot{\hat{\omega}}_m = \frac{\alpha_{11}}{\epsilon_1}(\omega_m - \hat{\omega}_m) + \dot{\omega}_m \\ \ddot{\hat{\omega}}_m = \dot{\Psi}_1 + \frac{\alpha_{12}}{\epsilon_1^2}(\omega_m - \hat{\omega}_m) + b1(0)u_1 \\ \dot{\hat{\Psi}}_1 = \frac{\alpha_{13}}{\epsilon_1^3}(\omega_m - \hat{\omega}_m) \end{cases} \quad (12)$$

where $\hat{\omega}_m$, $\dot{\hat{\omega}}_m$, $\ddot{\hat{\omega}}_m$ and $\dot{\hat{\Psi}}_1$ are the estimations of ω_m , $\dot{\omega}_m$, $\ddot{\omega}_m$ and $\dot{\Psi}_1$, respectively, and α_{11} , α_{12} and α_{13} are the positive constants and $0 < \epsilon_1 \ll 1$.

By using the estimated perturbations to compensate the actual perturbations, the control laws of the WT can be obtained as following:

$$u_1 = b1(0)^{-1}[-\hat{\Psi}_1 - k_{11}(\omega_m - \omega_m^*) - k_{12}(\dot{\hat{\omega}}_m - \dot{\omega}_m^*) + \ddot{\omega}_m^*] \quad (13)$$

where k_{11} and k_{12} are positive gains, and the poles of the closed-loop system are in the left-half plane (LHP).

For the PMSG, the system outputs are chosen as $y_{PMSG} = [y_2, y_3]^T = [i_{md}, i_{mq}]^T$, and i_{md}^* and i_{mq}^* are the reference values of stator currents i_{md} and i_{mq} , respectively. According to Equation (7), differentiate y_{PMSG} until the control input appears explicitly, it expresses as

$$\dot{y}_2 = \Psi_2 + b_2(0)u_2 \quad (14)$$

$$\dot{y}_3 = \Psi_3 + b_3(0)u_3 \quad (15)$$

where $b_2(0)$ and $b_3(0)$ are nominal values of $b_2(x) = \frac{1}{L_{md}}$, and $b_3(x) = \frac{1}{L_{mq}}$, respectively.

According to Equations (6) and (7), the perturbations are expressed as follows

$$\Psi_2 = \frac{1}{L_{md}}(-i_{md}R_s + \omega_e L_{mq}i_{mq}) + (b_2(x) - b_2(0))u_2 \quad (16)$$

$$\Psi_3 = -\frac{R_s}{L_{mq}}i_{mq} - \frac{1}{L_{mq}}\omega_e(L_{md}i_{md} + K_e) + (b_3(x) - b_3(0))u_3 \quad (17)$$

According Equation (9), two second-order perturbation observers (POs) for Ψ_2 and Ψ_3 estimation are designed, respectively:

$$\begin{cases} \dot{\hat{i}}_{md} = \hat{\Psi}_2 + \frac{\alpha_{21}}{\epsilon_2}(i_{md} - \hat{i}_{md}) + b_2(0)u_2 \\ \dot{\hat{\Psi}}_2 = \frac{\alpha_{22}}{\epsilon_2^2}(i_{md} - \hat{i}_{md}) \end{cases} \quad (18)$$

$$\begin{cases} \dot{\hat{i}}_{mq} = \hat{\Psi}_3 + \frac{\alpha_{31}}{\epsilon_2}(i_{mq} - \hat{i}_{mq}) + b_3(0)u_3 \\ \dot{\hat{\Psi}}_3 = \frac{\alpha_{32}}{\epsilon_2^2}(i_{mq} - \hat{i}_{mq}) \end{cases} \quad (19)$$

where \hat{i}_{md} , $\dot{\hat{i}}_{md}$, $\hat{\Psi}_2$, $\dot{\hat{\Psi}}_2$, \hat{i}_{mq} , $\dot{\hat{i}}_{mq}$ and $\hat{\Psi}_3$ are the estimations of i_{md} , \dot{i}_{md} , Ψ_2 , $\dot{\Psi}_2$, i_{mq} , \dot{i}_{mq} and Ψ_3 , respectively, and α_{21} , α_{22} , α_{31} and α_{32} are the positive constants.

The adaptive control of the PMSG employing the perturbation estimation is designed as

$$\begin{cases} u_2 = b_2(0)^{-1}(-\hat{\Psi}_2 - k_{21}(\hat{i}_{md} - i_{md}^*) + \dot{i}_{md}^*) \\ u_3 = b_3(0)^{-1}(-\hat{\Psi}_3 - k_{31}(\hat{i}_{mq} - i_{mq}^*) + \dot{i}_{mq}^*) \end{cases} \quad (20)$$

where k_{21} and k_{31} are positive feedback control gains, hence put the poles of the closed-loop system in the LHP.

Remark 1. *The adaption laws are developed based on quadratic Lyapunov function. The performance of adaptive control can be enhanced by using non-quadratic Lyapunov functions [44,51].*

3.2. Normal Operation

In normal operation, for the MSC, the MPPT algorithm reported in [47] is applied in extracting the maximum wind power under below-rated wind speeds. The mechanical rotation speed ω_m is required to track its optimal reference ω_{mopt} , while the d-axis stator current reference $i_{m\text{dr}}$ is 0. When the wind speeds are above the rated speed, the adaptive pitch control is employed to limit the captured power from wind. The extracted wind power should be maintained at its rated value. It in turn requires both the mechanical torque T_m and mechanical rotation speed ω_m to keep at their rated values, respectively.

For the GSC, the active power P_m generated by the PMSG is first transferred to DC-Link, then from DC-Link to grid. Two VSCs are controlled separately, and the dynamics of the PMSG-WT and power grid are decoupled via the DC-Link when DC-Link voltage V_{dc} is always maintained at its reference V_{dc}^* . To regulate the DC-Link voltage V_{dc} , an adaptive DC-Link voltage V_{dc} control strategy has been developed in [45]. In addition, the reference of the grid current in the q-axis i_{gq}^* is 0, grid voltage in the d-axis E_{gd} is rated voltage, and the grid voltage in the q-axis E_{gq} is 0. The injected grid reactive power Q_g should be around 0 when GSC controller can realize its control objectives.

3.3. Operation Under Grid Voltage Dips

Under the grid voltage dips, the GSC adopts the same control strategy as normal operation. Both the reactive and active current of the GSC required by the fault ride-through of the grid codes have not been applied in GSC controller. The DC-Link voltage V_{dc} is required to be kept at its rated value. It will not absorb excess active power. For the MSC, the generating active power is still delivering to the grid during the grid voltage E_{gd} dips. The generated active power P_m is the same as the injected grid active power P_g when MSC controller does not take any control action. The grid current i_{gd} will increase rapidly when the DC-Link voltage V_{dc} is well regulated under the grid voltage dips. This may damage VSCs or other power electronic devices. Hence, the active power exported by the WECS should be in proportion to the level of the retained grid voltage. The damage of the GSC caused by the large inrush current during the grid voltage dips can be prevented [25,29]. When the grid voltage dips are detected, the generated active power P_m should reduce simultaneously [39]. For this reason, pitch control is employed to assist in reducing generated active power P_m in this paper. When the pitch control is applied in MSC under grid voltage dips, the mechanical rotation speed reference ω_m^* (FRTC) is the same as normal operation. However, the electromagnetic torque reference T_{er} is in proportion to the level of the retained grid voltage shown in (21).

$$T_{er} = \frac{E_{gd}(t)}{E_{gd}(0)} T_{er\text{normal}} \quad (21)$$

where T_{er} is the electromagnetic torque reference applied in pitch control when the grid voltage dips; $E_{gd}(t)$ is the value of the grid voltage after the grid voltage dips; $E_{gd}(0)$ is the rated grid voltage; and $T_{er\text{normal}}$ is the electromagnetic torque in normal operation.

According to (2), the q-axis stator current reference i_{mq}^* (FRTC) applied in pitch control is $\frac{E_{gd}(t)}{E_{gd}(0)pK_e} T_{er\text{normal}}$.

The overall control structure of adaptive control-based GSC and MSC for the WECS based on PMSG is shown in Figure 3.

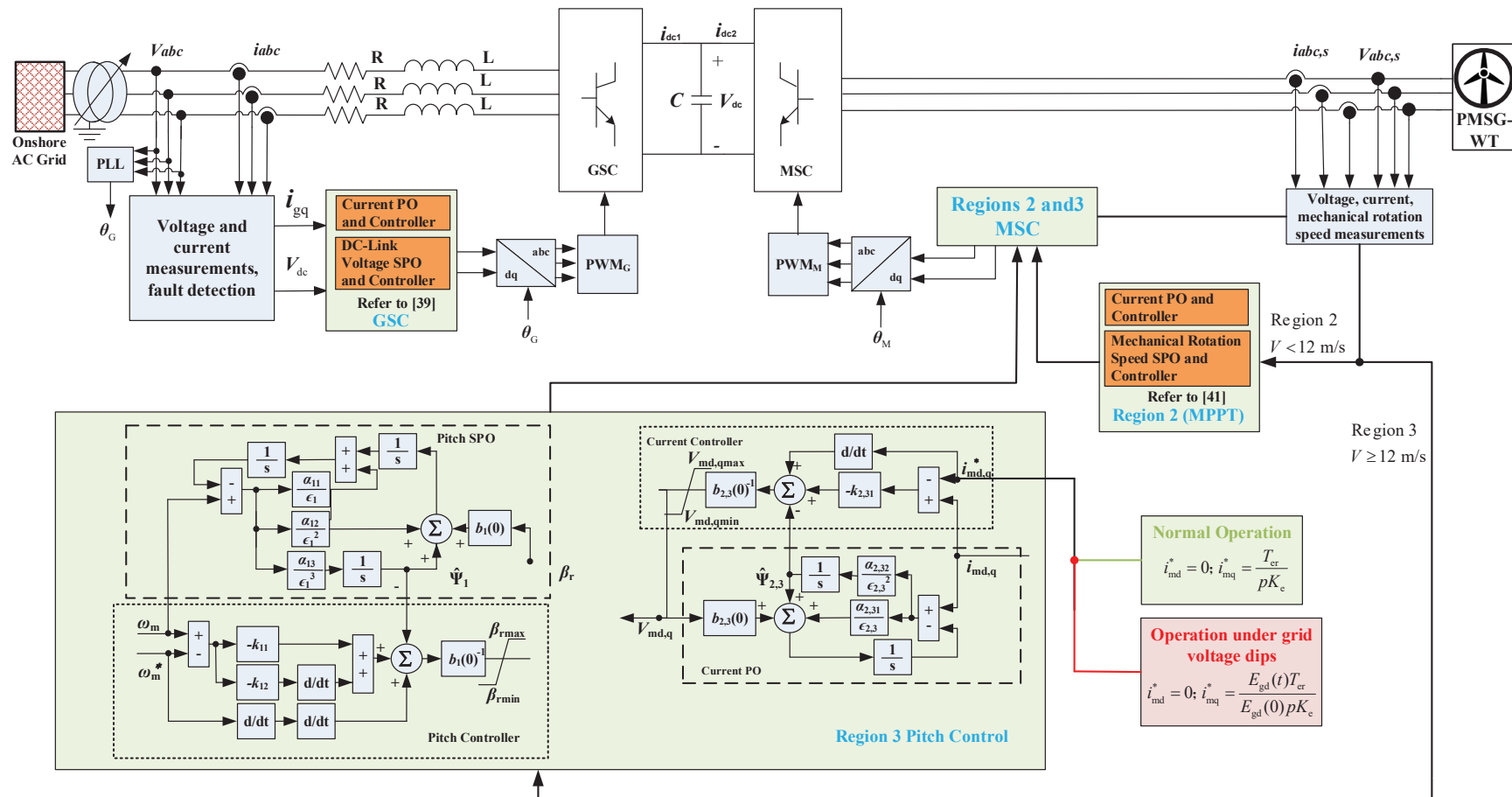


Figure 3. The overall control structure of the adaptive control-based GSC and MSC for the WECS based on PMSG.

4. Simulation Results

To verify the effectiveness of the proposed adaptive control approach, a series of simulations studies are carried out, and the VC and FLC are employed for comparisons. A 2-MW WECS is investigated. The parameters of the PMSG-WT system are $\rho = 1.205 \text{ kg/m}^3$, $R = 39 \text{ m}$, rated wind speed $V_r = 12 \text{ m/s}$, $J_{\text{tot}} = 1 \times 10^4 \text{ kg} \cdot \text{m}^2$, $K_e = 136.25 \text{ V}\cdot\text{s/rad}$, $p = 11$, $L_{\text{md}} = 5.5 \times 10^{-3} \text{ H}$, $L_{\text{mq}} = 3.75 \times 10^{-3} \text{ H}$, and $R_s = 5 \times 10^{-5} \Omega$; the parameters of the grid are $L_g = 6.31 \times 10^{-5} \text{ H}$, $C = 0.06 \text{ F}$, and $R_g = 1.98 \times 10^{-3} \Omega$.

The parameters of adaptive controller for the GSC are the same as listed in [45]. For the MSC, the parameters of adaptive controller aiming to extract the maximum wind power under below-rated wind speeds are the same as listed in [47]. The adaptive pitch controller parameters are listed in Table 1. Note that the FLC uses the same controller parameters as the PO-AC, moreover the FLC uses the full state measurements except $\frac{dV}{dt}$ and the exact parameters.

Table 1. Parameters of adaptive pitch control.

Parameters of the adaptive controller	
Gains of observer (12)	$\alpha_{11} = 50, \alpha_{12} = 1.875 \times 10^3, \alpha_{13} = 1.5625 \times 10^4, \epsilon_1 = 0.02$
Gains of observer (18)	$\alpha_{21} = 4 \times 10^2, \alpha_{22} = 4 \times 10^4, \epsilon_2 = 0.01$
Gains of observer (19)	$\alpha_{31} = 4 \times 10^2, \alpha_{32} = 4 \times 10^4, \epsilon_3 = 0.01$
Gains of linear controller	$k_{11} = 4 \times 10^2, k_{12} = 40, k_{21} = 1.6 \times 10^2, k_{31} = 1.6 \times 10^2$

4.1. Ramp Wind Speed

The responses of the WT to ramp wind speed is shown in Figure 4. Wind speed is shown in Figure 4a. Under the above-rated wind speeds, among these three controllers, the worst tracking performance of the mechanical rotation speed ω_m with the longest recovery time and biggest overshoots is achieved by the VC. The maximum tracking error ($\frac{\omega_m - \omega_{mr}}{\omega_{mr}} \times 100\%$) is more than 15% under the VC. The tracking error of the ω_m still exists under the FLC. The best tracking performance is provided by the PO-AC. Under the below-rated wind speeds, both the FLC and PO-AC provide satisfactory tracking performances of the ω_m . However, the VC still has tracking error of the ω_m . It can be explained that the VC is designed based on one specific operation point and cannot provide optimal performance in the whole operation region. The FLC exists tracking error under the above-rated wind speeds, because the $\frac{dV}{dt}$ is unknown in the FLC design. Under the below-rated wind speeds, the FLC knows the full state measurements and accurate system parameters. Hence, high performance is achieved by the FLC.

Under the above-rated wind speeds, the pitch angle β_r changes with the varying wind speeds to limit the extracted wind power. Under the below-rated wind speeds, the pitch angle β_r is constant. The response of the β_r is shown in Figure 4d. When the wind speed decreases from 14 m/s to 12 m/s, the pitch angle reference β_r value also decreases. It is because that the captured wind power decreases with the decreasing wind speed when the pitch angle reference β_r does not change. To keep the captured wind power at rated power, the pitch angle should decrease for increasing the power coefficient C_p . Under the above-rated wind speeds, comparing with the FLC or PO-AC, the VC requires more time to reach the expected β_r . Figure 4e–h show the responses of the power coefficient C_p , T_m and T_e to ramp wind speed. In Figure 4e, the power coefficient C_p increases with decreasing pitch angle reference β_r . The expected wind power can be achieved by the PO-AC even when wind speed varies, that neither the VC nor FLC can provide, as shown in Figure 4h.

The responses of the PMSG to ramp wind speed are shown in Figure 5. Figure 5a,b show that larger overshoots and longer recovery time of the stator voltages $V_{\text{md,q}}$ are obtained by the VC comparing with the FLC or PO-AC. In addition, the PO-AC obtains the best performance. The stator current i_{md} can be well tracked by these three controllers shown in Figure 5c. Figure 5d shows the response of i_{mq} .

The active and reactive power of the PMSG (P_m , Q_m) are shown in Figure 5e,f, respectively. It can be seen from Figure 5e that, when the wind speed is above-rated wind speeds, the rated electrical power can be always achieved by the PMSG under the PO-AC. Under below-rated wind speed, the generating power by the PMSG changes with varying wind speed.

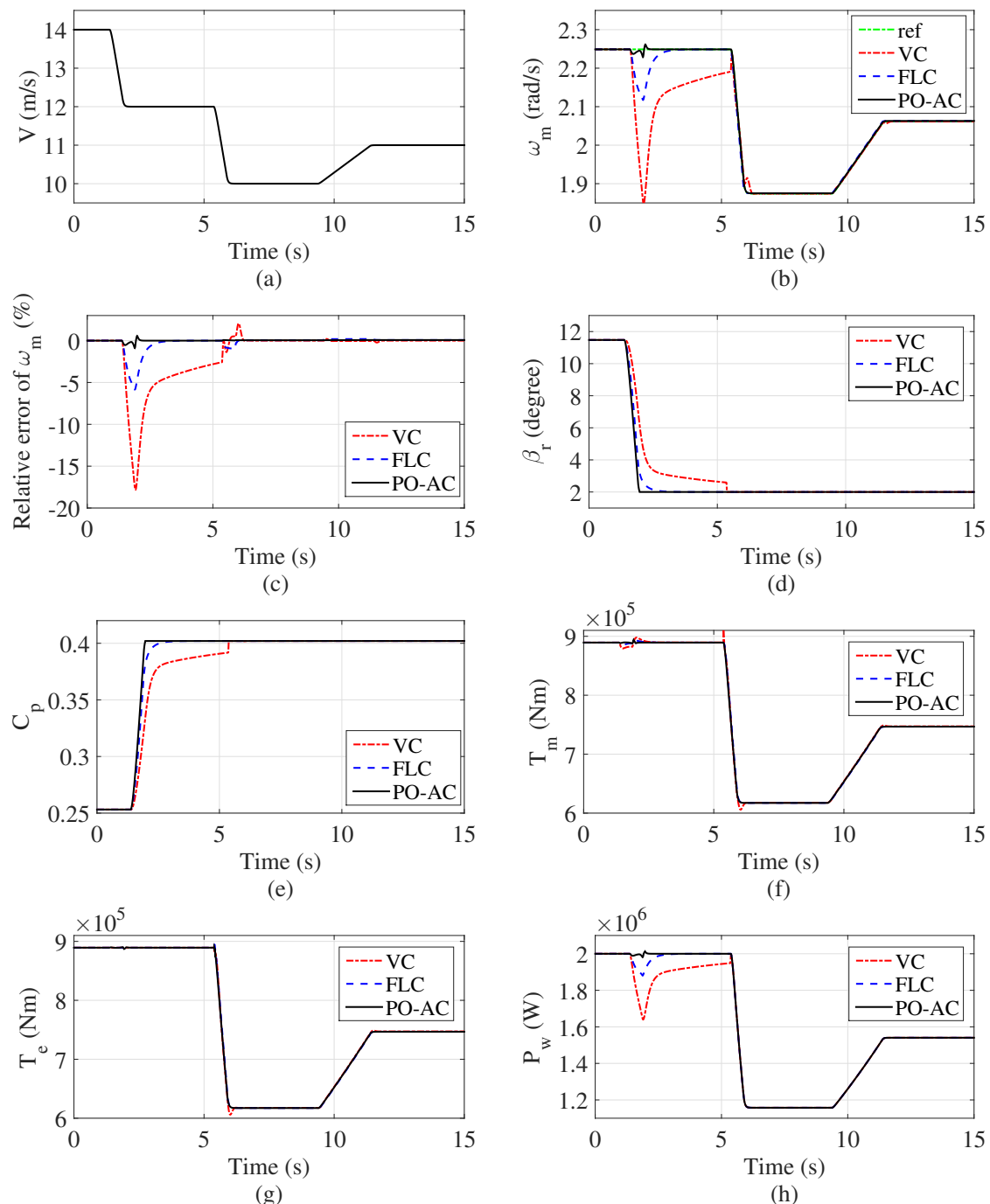


Figure 4. Responses of the WT to ramp wind speed. (a) Wind speed V . (b) Mechanical rotation speed ω_m . (c) Relative error of mechanical rotation speed ω_m . (d) Pitch angle reference β_r . (e) Power coefficient C_p . (f) Mechanical rotation torque T_m . (g) Electromagnetic torque T_e . (h) Mechanical power P_w .

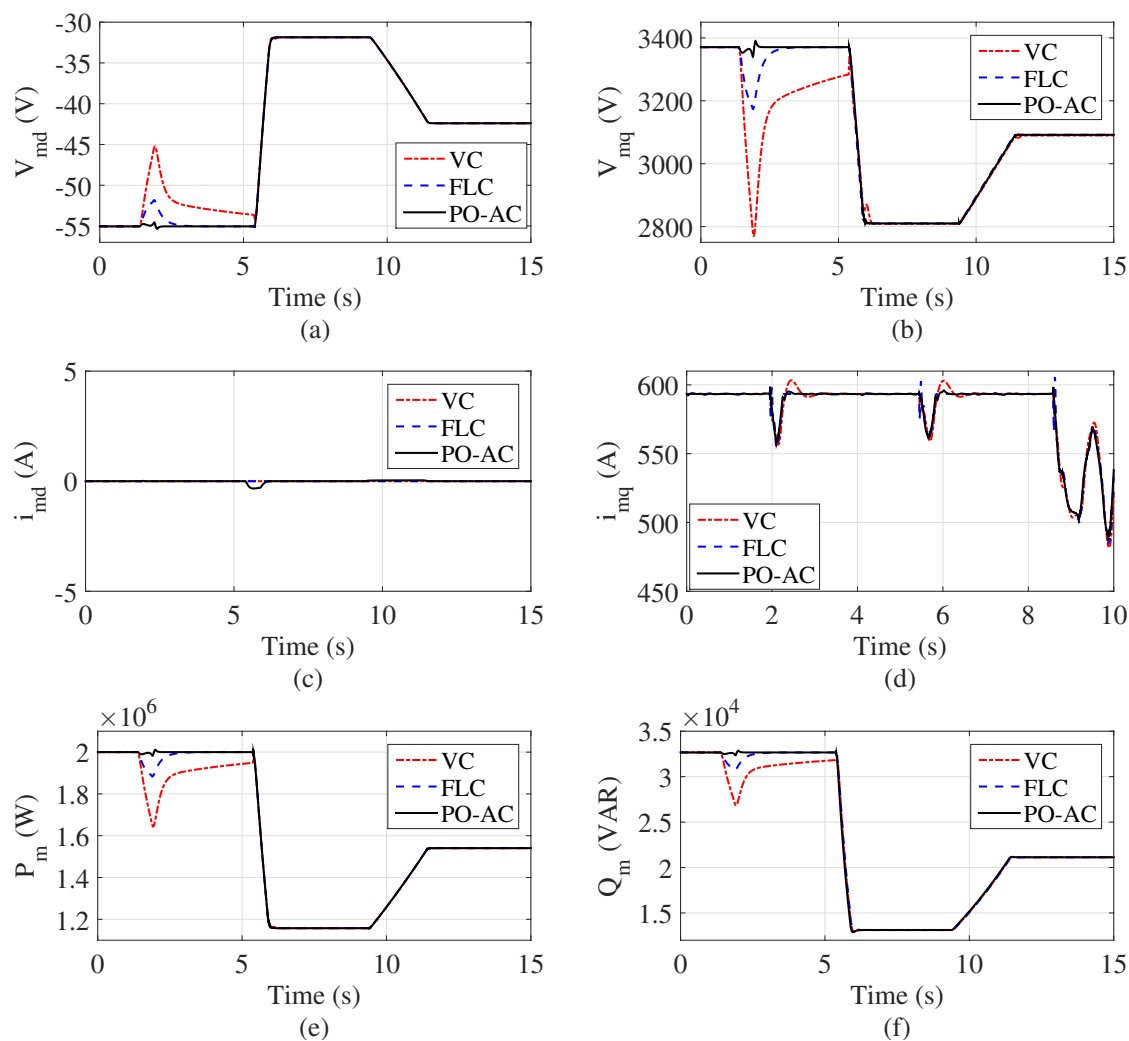


Figure 5. Responses of the PMSG to ramp wind speed. (a) d-axis voltage V_{md} . (b) q-axis voltage V_{mq} . (c) d-axis current i_{md} . (d) q-axis current i_{mq} . (e) Active generating power P_m . (f) Reactive generating power Q_m .

Figure 6 shows the responses of the grid to ramp wind speed. The q-axis current i_{gq} can be almost maintained around 0 by these three controllers shown in Figure 6a. To decouple the control of GSC and MSG, the DC-Link voltage V_{dc} should be maintained at 1500 V. It can be seen from Figure 6b that, the VC has larger overshoots and longer recovery time of the DC-Link voltage V_{dc} . The injected active power P_g and reactive power Q_g of the grid are shown in Figure 6c,d, respectively. Figure 6c,d show that the decoupled control for reactive and active power of grid can be realised.

During the whole operating period, the PO-AC can always keep consistent responses of P_m , Q_m , P_g and Q_g . The performances of the VC and FLC are affected by the varying wind speed. Note that the FLC uses the full state feedback except $\frac{dV}{dt}$ under above-rated wind speeds and extract parameters of the system, but the PO-AC is without requiring the details of the system information and extract parameters.

The estimates of the states and perturbations are shown in Figure 7. It shows that both the states and perturbations can be well estimated by the designed observers. The estimated perturbations including nonlinearities, uncertainties and disturbance are used for compensations of the real perturbations.

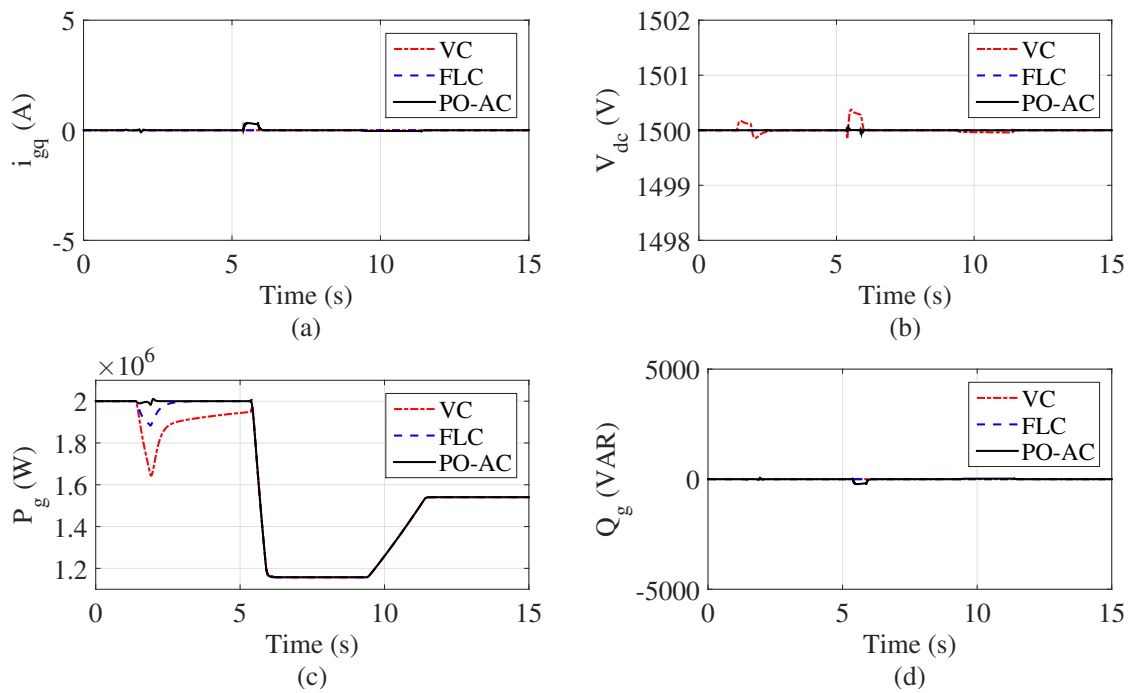


Figure 6. Responses of the grid to ramp wind speed. (a) q-axis current i_{gq} . (b) DC-Link voltage V_{dc} . (c) Active power of grid P_g . (d) Reactive power of grid Q_g .

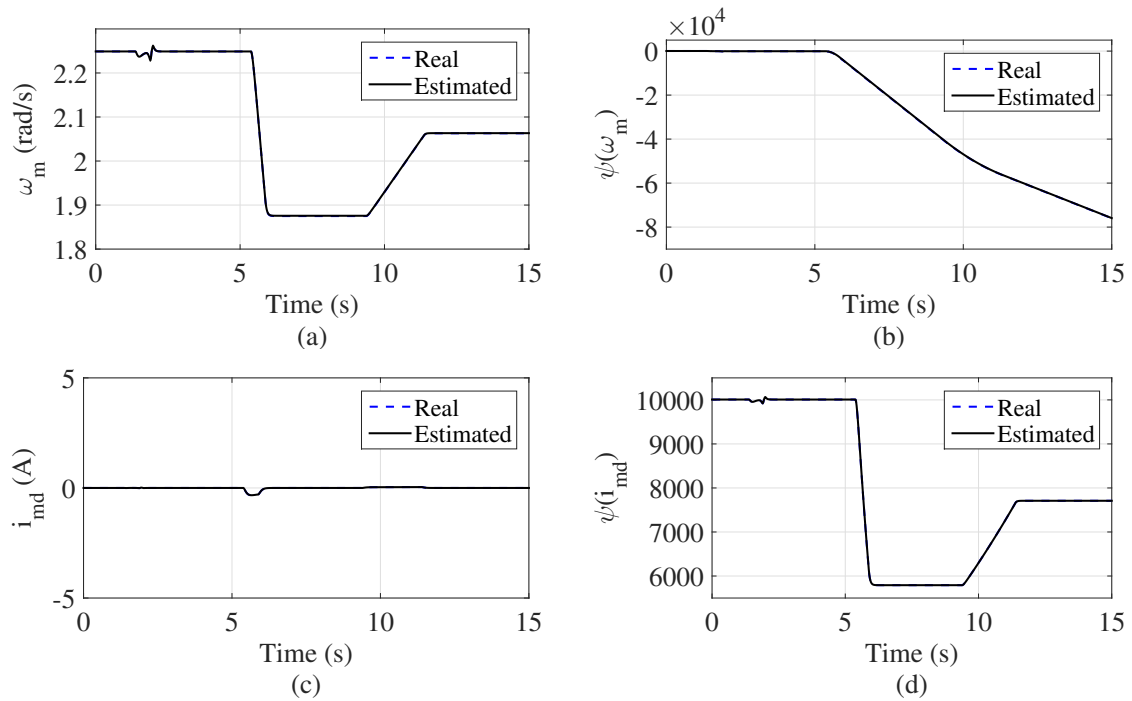


Figure 7. Cont.

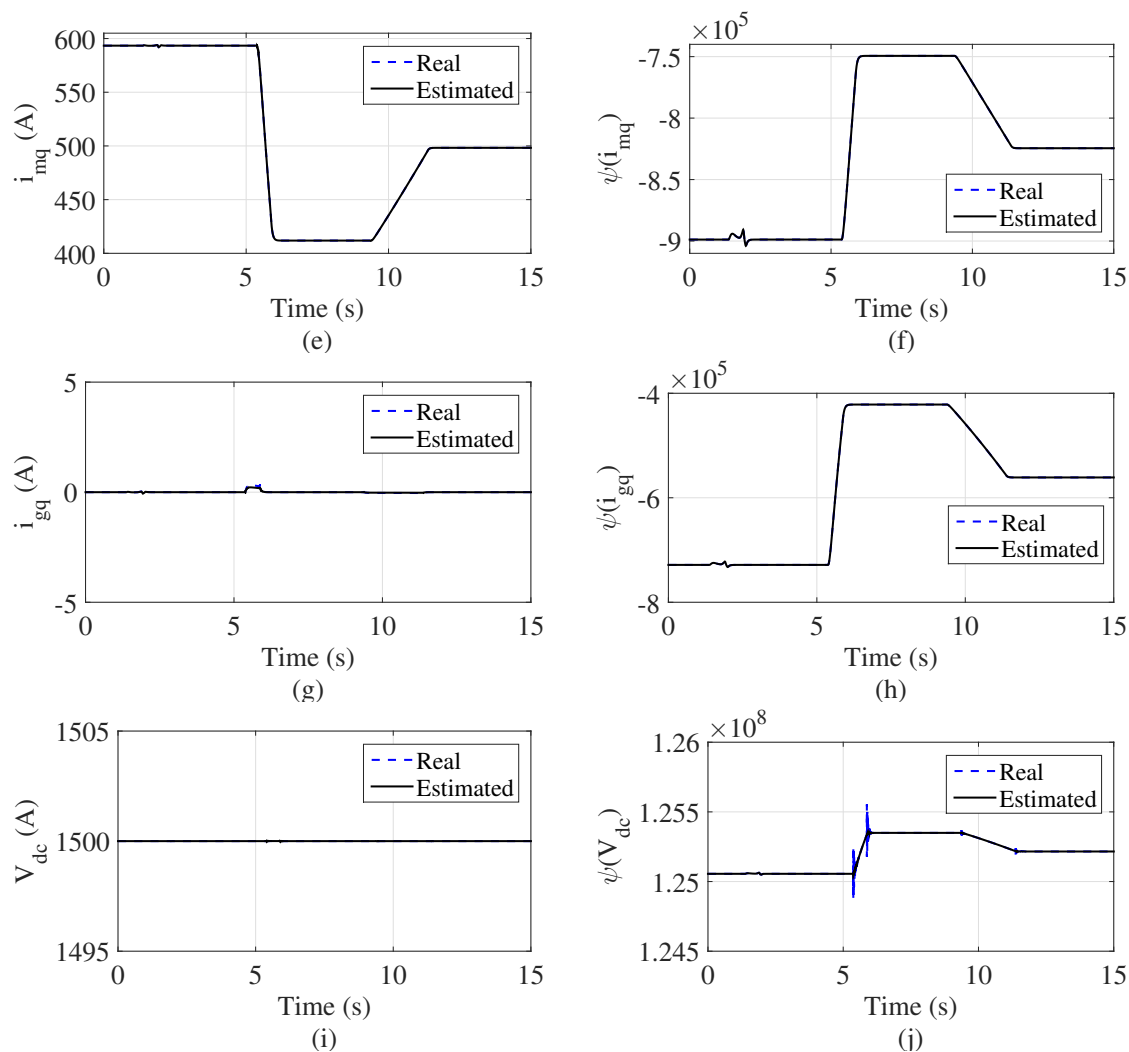


Figure 7. Estimates of states and perturbations to ramp wind speed. (a) Estimation of mechanical rotation speed ω_m . (b) Estimation of perturbation term $\Psi(\omega_m)$. (c) Estimation of i_{md} . (d) Estimation of perturbation term $\Psi(i_{md})$. (e) Estimation of i_{mq} . (f) Estimation of perturbation term $\Psi(i_{mq})$. (g) Estimation of i_{gq} . (h) Estimation of perturbation term $\Psi(i_{gq})$. (i) Estimation of V_{dc} . (j) Estimation of perturbation term $\Psi(V_{dc})$.

4.2. Random Wind Speed

The responses of the WT to random wind speed are shown in Figure 8. Wind speed is shown in Figure 8a. When wind speed is time-varying, neither the VC nor FLC can provide satisfactory tracking performances of the mechanical rotation speed ω_m shown in Figure 8b. The PO-AC always keeps ω_m around reference mechanical rotation speed. It can be seen from Figure 8c that, the maximum tracking errors ($\frac{\omega_m - \omega_{mr}}{\omega_{mr}} \times 100\%$) are approximately 13% and 5% under the VC and FLC, respectively. The pitch angle reference β_r and power coefficient C_p should change with the time-varying wind speeds under above-rated wind speeds, and keep constant under below-rated wind speeds. Figure 8d,e show that, the corresponding pitch angle reference β_r and power coefficient C_p can be achieved under time-varying wind speeds. Figure 8f–h show the responses of mechanical torque T_m , electromagnetic T_e , and mechanical power P_w , respectively.

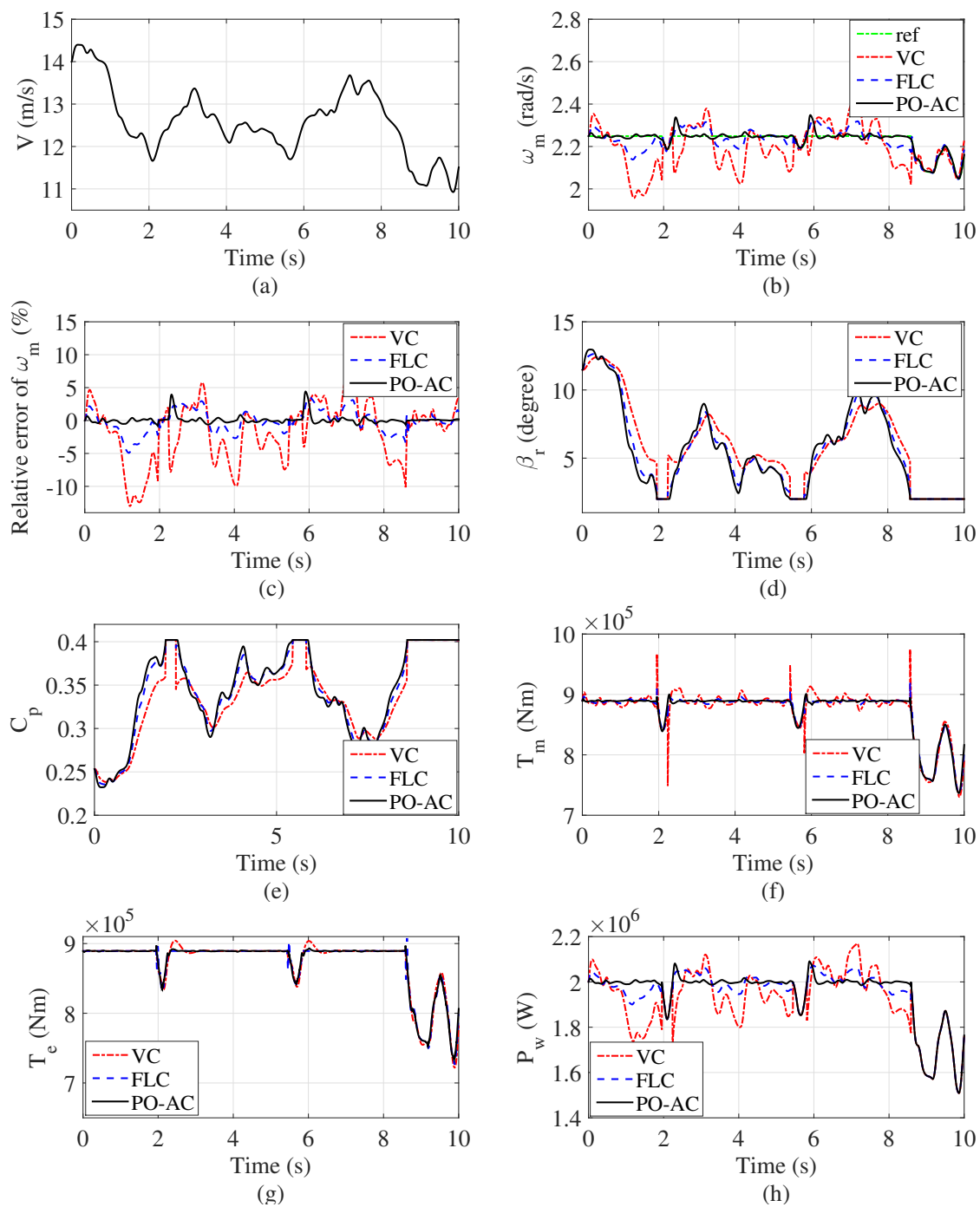


Figure 8. Responses of the WT to random wind speed. (a) Wind speed V . (b) Mechanical rotation speed ω_m . (c) Relative error of mechanical rotation speed ω_m . (d) Pitch angle reference β_r . (e) Power coefficient C_p . (f) Mechanical rotation torque T_m . (g) Electromagnetic torque T_e . (h) Mechanical power P_w .

Figure 9 shows the responses of the PMSG to random wind speed. During the whole operating period, the PO-AC can always keep consistent responses of P_m and Q_m . The performances of the VC and FLC are affected by the time-varying wind speeds. In Figure 10, the rated value of the DC-Link voltage V_{dc} can be achieved, and the control for reactive and active power of grid is well decoupled. In Figure 11, it shows that the observers can provide satisfactory estimations of the states and perturbations for compensating the real perturbations.

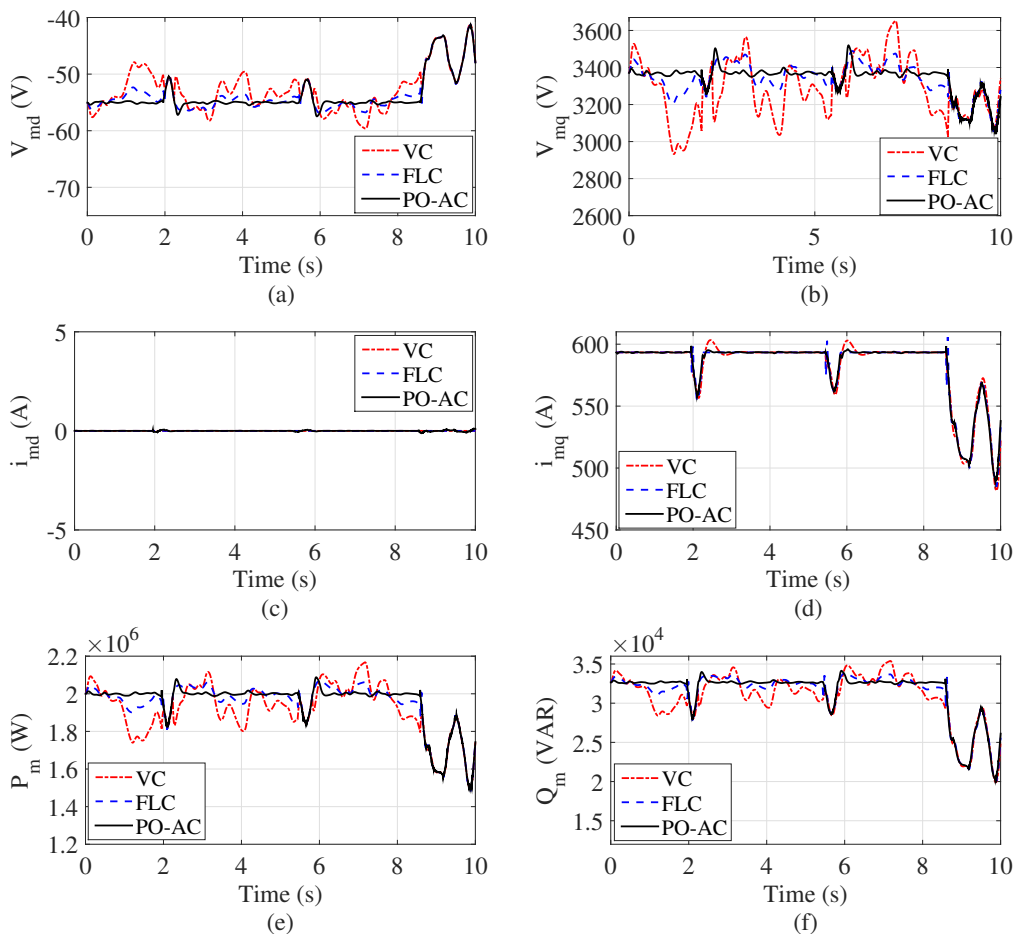


Figure 9. Responses of the PMSG to random wind speed. (a) d-axis voltage V_{md} . (b) q-axis voltage V_{mq} . (c) d-axis current i_{md} . (d) q-axis current i_{mq} . (e) Active generating power P_m . (f) Reactive generating power Q_m .

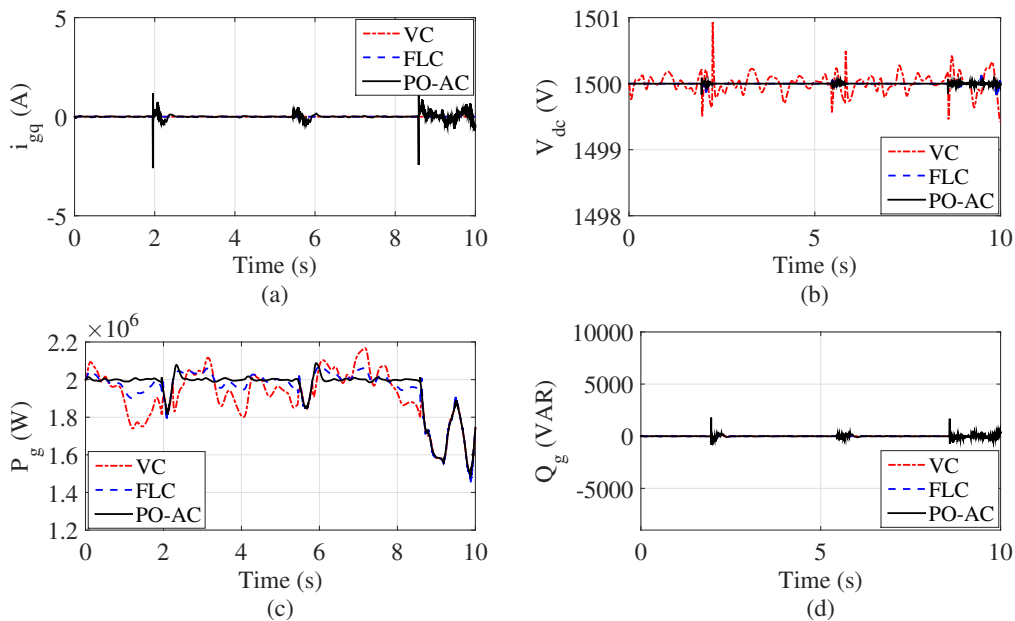


Figure 10. Responses of the grid to random wind speed. (a) q-axis current i_{gq} . (b) DC-Link Voltage V_{dc} . (c) Active power of grid P_g . (d) Reactive power of grid Q_g .

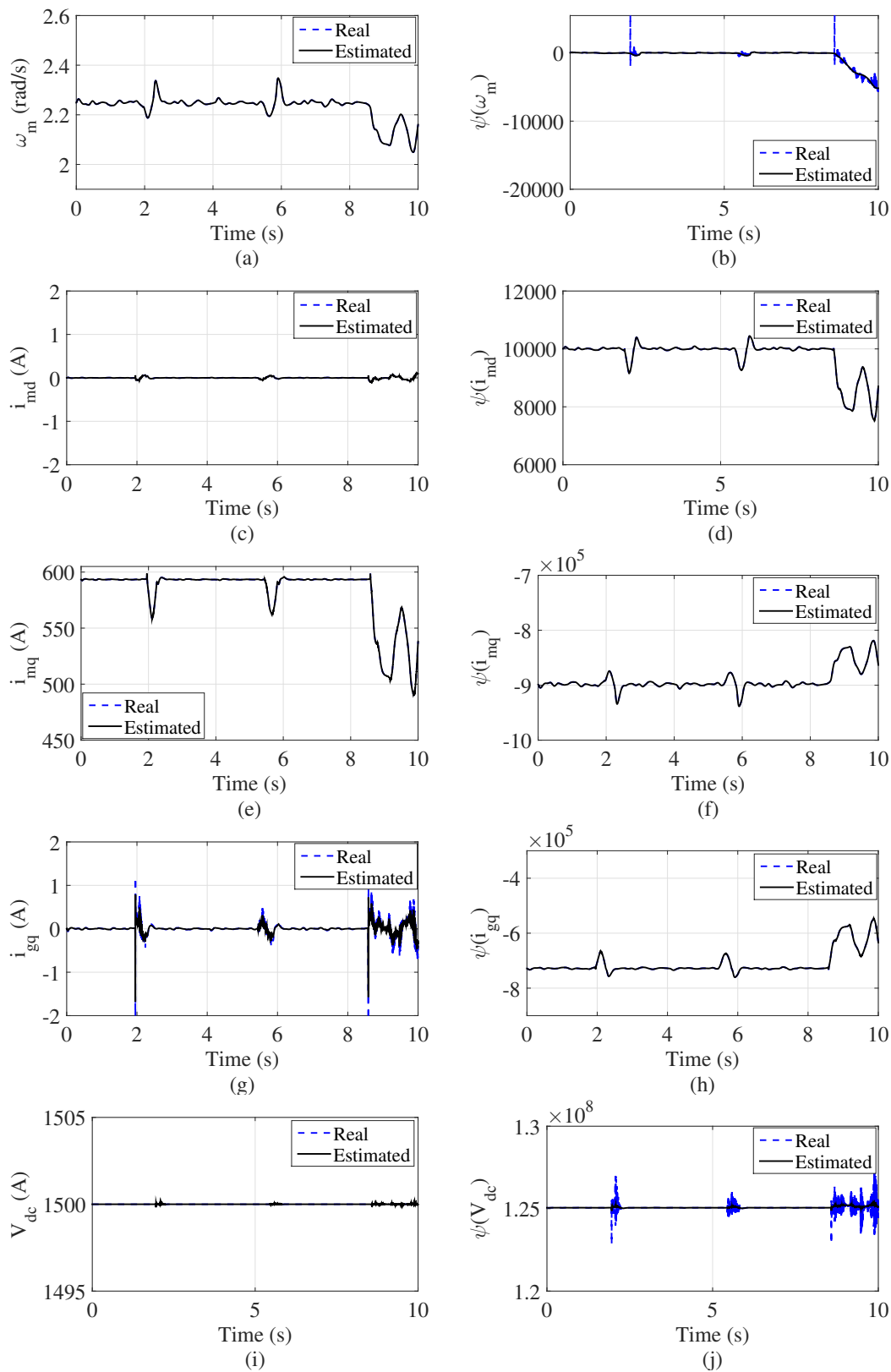


Figure 11. Estimates of states and perturbations to random wind. (a) Estimation of mechanical rotation speed ω_m . (b) Estimation of perturbation term $\Psi(\omega_m)$. (c) Estimation of i_{md} . (d) Estimation of perturbation term $\Psi(i_{md})$. (e) Estimation of i_{mq} . (f) Estimation of perturbation term $\Psi(i_{mq})$. (g) Estimation of i_{gq} . (h) Estimation of perturbation term $\Psi(i_{gq})$. (i) Estimation of V_{dc} . (j) Estimation of perturbation term $\Psi(V_{dc})$.

4.3. FRTC Compliance With the Pitch Control

During grid voltage dips, if the extracted wind power does not change, the grid current i_{gd} increases sharply under well control of the DC-Link voltage V_{dc} . The fast increasing grid current i_{gd} may damage the devices. If the extracted wind power can be reduced immediately as grid voltage dips, the increasing grid current i_{gd} can be reduced. To reduce the wind power captured by the WT, the power coefficient is decreased by using pitch control. By using this control strategy, it can assist the WECS in protecting the devices and improving the FRTC of the WECS.

When the grid voltage dips are detected, the pitch control is applied to reduce the captured wind power. When pitch control strategy is applied, the mechanical rotational speed ω_m should keep constant, and the mechanical torque T_m is reduced to the required value. However, the mechanical rotational speed ω_m increases when pitch control strategy is applied to reduce the captured wind power, as shown Figure 12c. It is because that the pitch angle rate is limited in the range ± 20 degree/s under the emergency condition [52,53]. From Figure 12d, it can be seen that the pitch angle reference β_r rate is much higher than ± 20 degree/s under the FLC and PO-AC. Hence, the real pitch angle β applied to the WT cannot be the same as the β_r due to pitch angle rate limit. It in turn results in the increment of the ω_m . The excess wind power is stored in the rotor inertia. Figure 12e shows the power coefficient C_p can be reduced by varying pitch angle. The decrement of the C_p is much larger under the FLC and PO-AC than the VC. It can be explained that the VC has much slower response of the β compared to the FLC or PO-AC. If the β cannot decrease quickly, the C_p cannot decrease immediately. Both the T_m and T_e have fast decrements under the FLC and PO-AC, as shown in Figure 12f,g. However, the VC has smaller reduction and longer recovery time. Figure 12h shows both the PO-AC and FLC have larger reduction of captured wind power P_w than the VC under grid voltage dips.

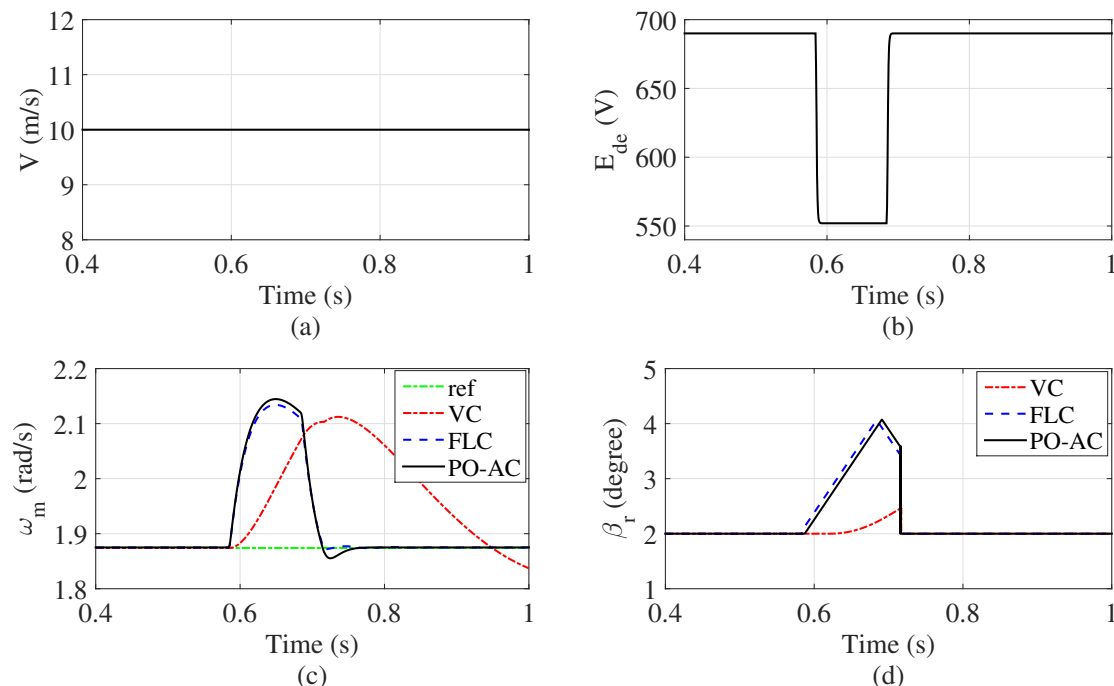


Figure 12. Cont.

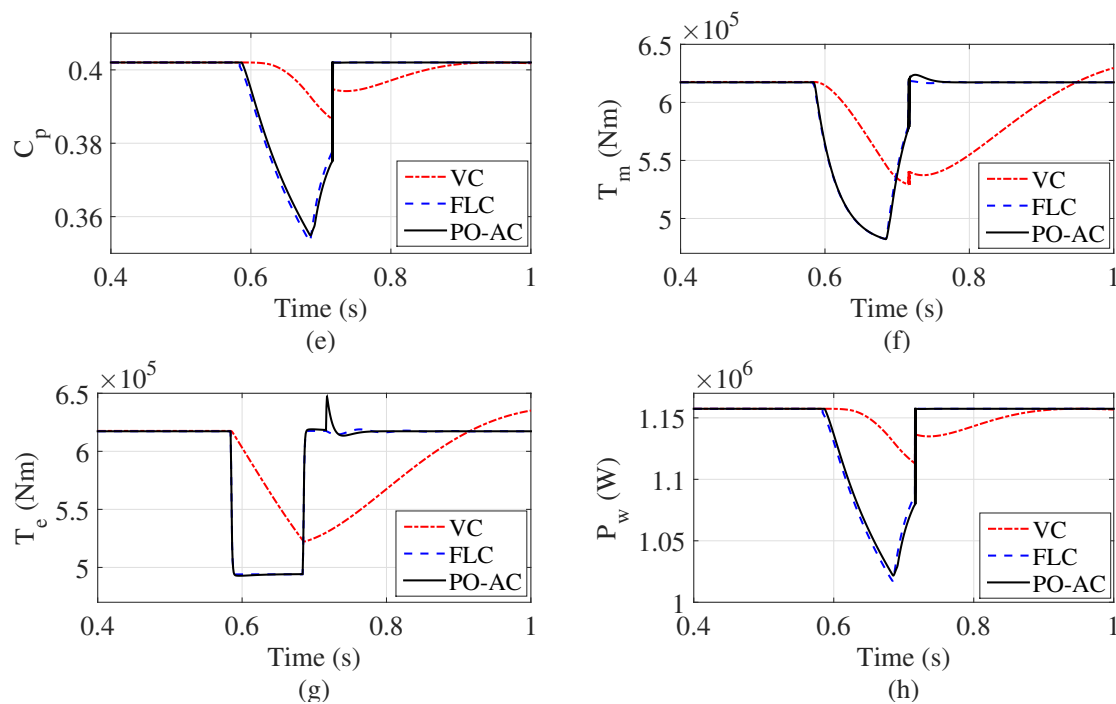


Figure 12. Responses of the WT to constant wind speed with protection under grid voltage dips. (a) Wind speed V . (b) Grid Voltage E_{gd} . (c) Mechanical rotation speed ω_m . (d) Pitch angle reference β_r . (e) Power coefficient C_p . (f) Mechanical rotation torque T_m . (g) Electromagnetic torque T_e . (h) Mechanical power P_w .

The responses of the PMSG to constant wind speed with protection under grid voltage dips are shown in Figure 13. When the grid voltage dips, the electromagnetic torque reference T_{er} is reduced proportionally to the grid voltage dips to keep balance between the generating power P_m and injected grid power P_g . It in turn limits the increasing grid current i_{gd} for protecting the devices. If the stator current i_{md} is well controlled, the T_e is proportional to the i_{mq} . However, it can be seen from Figure 13d that, the i_{mq} cannot track its reference under the VC. Both the FLC and PO-AC provide satisfactory tracking performance of i_{mq} . Figure 13e shows the active generating power P_m has bigger reduction with shorter recovery time under the FLC and PO-AC than that under the VC.

Figure 14 shows the responses of the grid under grid voltage dips. It can be seen from Figure 14 that, the grid current i_{gd} achieve smaller current under the FLC and PO-AC than that achieved under the VC when grid voltage dips occur. When pitch control strategy is applied under grid voltage dips, the i_{gd} can be reduced to approximately 1300A under the FLC and PO-AC, as shown in Figure 14. However, the VC does not limit the i_{gd} significantly as FLC or PO-AC. Compared with the VC, the DC-Link voltage V_{dc} has smaller overshoots and shorter recovery time under the FLC and PO-AC. When pitch control strategy is applied, the injected active power of grid P_g has bigger reduction under the FLC and PO-AC compared to the VC. The FRTC of the WECS can be enhanced by using the pitch control strategy based on the FLC or PO-AC. In Figure 15, it shows that the estimations of the states and perturbations can be well estimated to compensate the real perturbations.

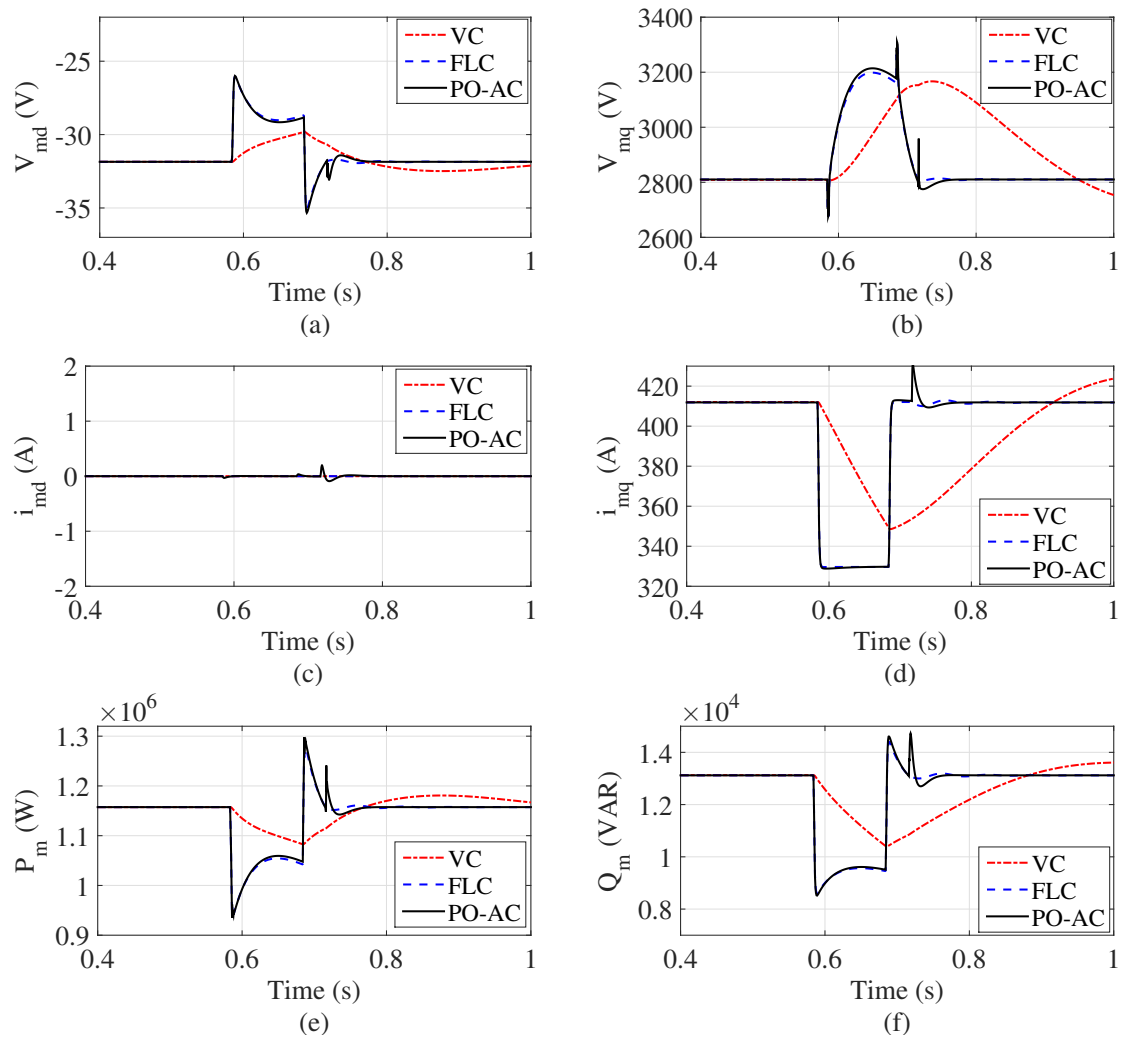


Figure 13. Responses of the PMSG to constant wind speed with protection under grid voltage dips. (a) d-axis voltage V_{md} . (b) q-axis voltage V_{mq} . (c) d-axis current i_{md} . (d) q-axis current i_{mq} . (e) Active generating power P_m . (f) Reactive generating power Q_m .

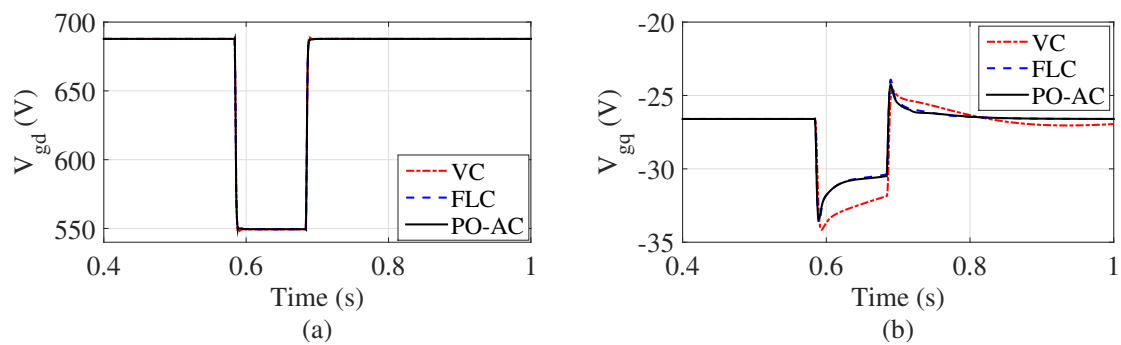


Figure 14. Cont.

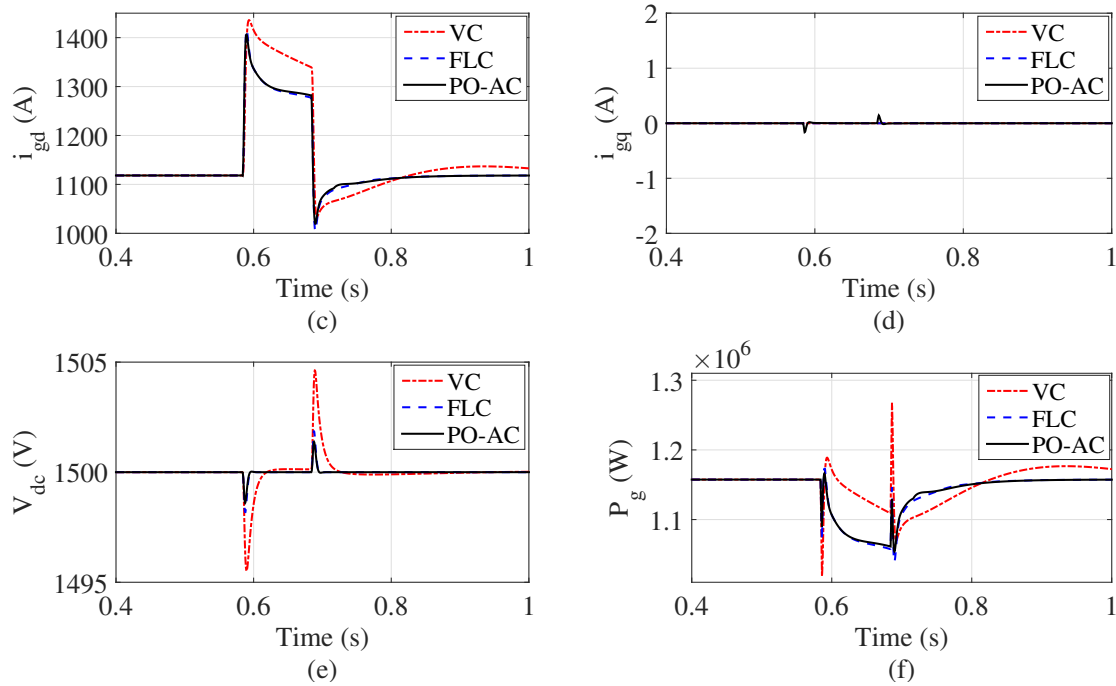


Figure 14. Responses of the grid to constant wind speed with protection under grid voltage dips. (a) d-axis voltage V_{gd} . (b) q-axis voltage V_{gq} . (c) d-axis current i_{gd} . (d) q-axis current i_{gq} . (e) DC-Link Voltage V_{dc} . (f) Active grid power P_g .

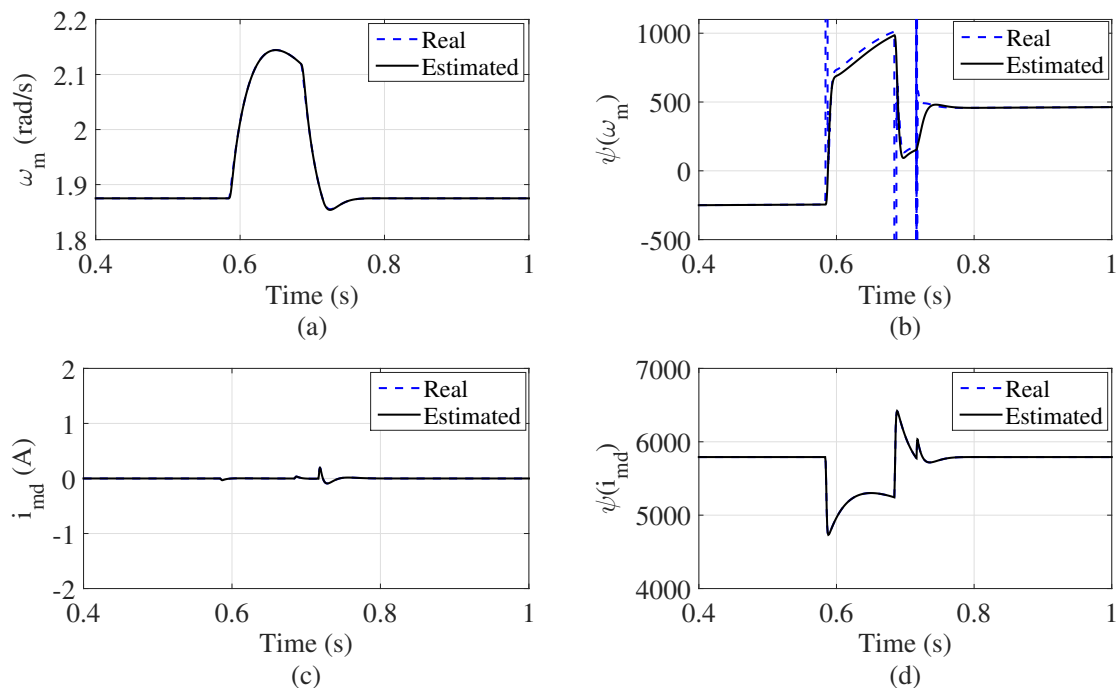


Figure 15. Cont.

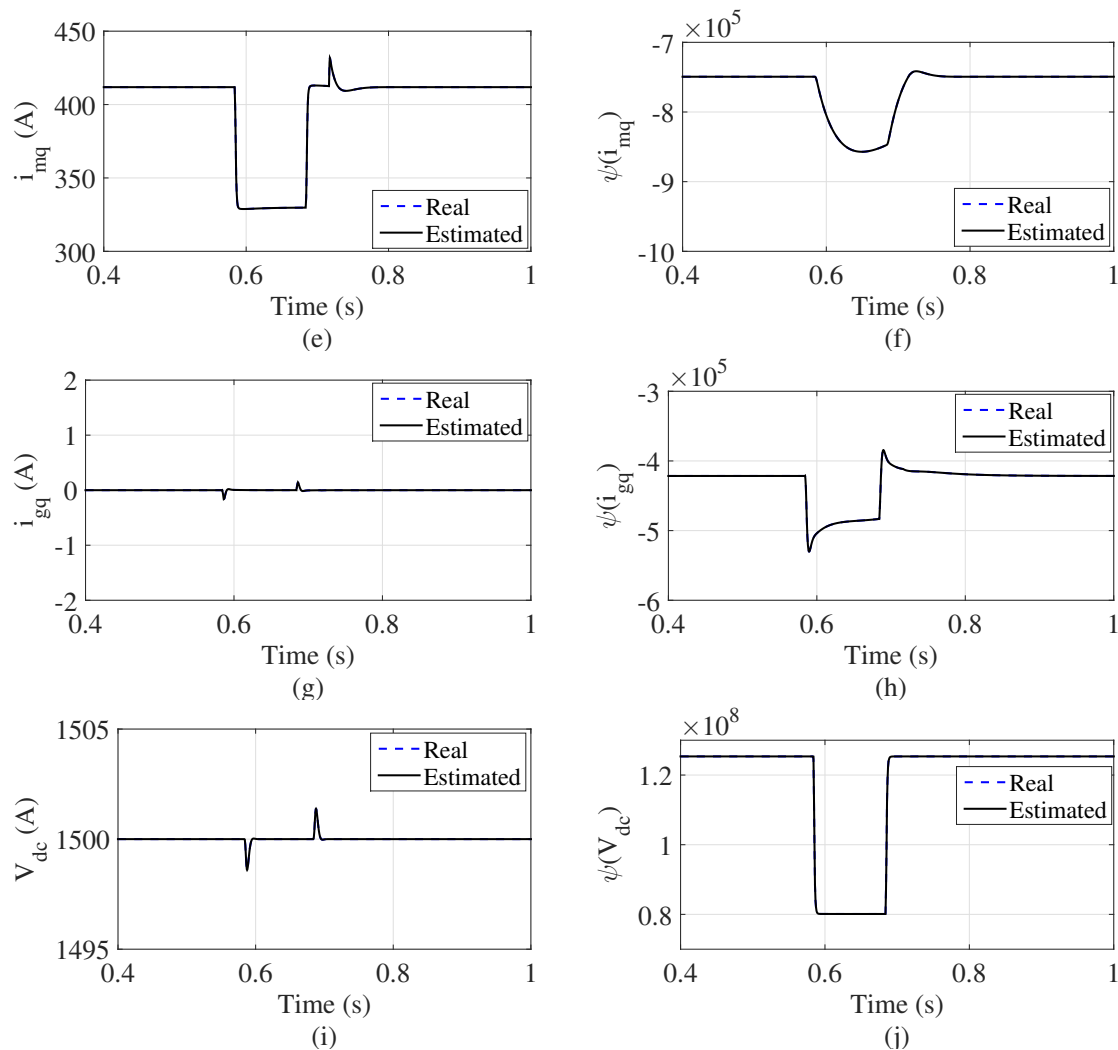


Figure 15. Estimates of states and perturbations to constant wind speed with protection under grid voltage dips. (a) Estimation of mechanical rotation speed ω_m . (b) Estimation of perturbation term $\Psi(\omega_m)$. (c) Estimation of i_{md} . (d) Estimation of perturbation term $\Psi(i_{md})$. (e) Estimation of i_{mq} . (f) Estimation of perturbation term $\Psi(i_{mq})$. (g) Estimation of i_{gq} . (h) Estimation of perturbation term $\Psi(i_{gq})$. (i) Estimation of V_{dc} . (j) Estimation of perturbation term $\Psi(V_{dc})$.

In addition, the control performances of these three controllers via integral of absolute error (IAE) in different simulation scenarios are shown in Table 2. Here, $IAE_x = \int_0^T |x - x^*|$. The reference value of the variable x is x^* . The simulation time T is set as 15s, 10s and 1s in these three simulation scenarios, respectively. It can be seen from Table 2 that, in first and second simulation scenarios, the IAE_{ω_m} and $IAE_{V_{dc}}$ achieves the smallest values under the PO-AC. In the FRTC compliance with the pitch control simulation scenario, both the PO-AC and FLC provide much smaller IAE_{ω_m} , $IAE_{i_{gq}}$ and $IAE_{V_{dc}}$ than those achieved by the VC.

Table 2. IAE indices of different controllers in different scenarios.

Simulation Scenarios	Variables	Controllers		
		VC	FLC	PO-AC
Ramp wind speed	IAE_{ω_m} (rad)	0.5116	0.09338	0.01746
	$IAE_{i_{mq}}$ (A.s)	10.46	13.25	11.15
	$IAE_{V_{dc}}$ (V.s)	0.3654	7.616×10^{-3}	2.521×10^{-3}
Random wind speed	IAE_{ω_m} (rad)	0.814	0.2949	0.06717
	$IAE_{i_{mq}}$ (A.s)	41.84	10.84	9.173
	$IAE_{V_{dc}}$ (V.s)	1.054	0.02976	0.01186
FRTC compliance with the pitch control	IAE_{ω_m} (rad)	0.04794	0.02485	0.02611
	$IAE_{i_{mq}}$ (A.s)	30.19	0.2657	0.393
	$IAE_{V_{dc}}$ (V.s)	0.1299	0.01892	0.01419

5. Conclusions

This paper has proposed a PO-AC for the GSC and MSC of the WECS based on PMSG. The objectives of different operation conditions can be achieved by using the PO-AC, e.g., extract the maximum wind power under the below-rated wind speeds, limit the extracted wind power under the above-rated wind speeds, and regulate the DC-Link voltage and decouple the reactive and active power injected into the grid. It provides better performances of the WECS than the VC designed based on optimal operating point and FLC requiring full state measurements and accurate system model. In addition, the pitch control strategy has been employed to assist in reducing the extracted wind power for enhancing the FRTC of the WECS. In the further work, the adaptive control strategy based on grid code requirement can be applied for improving the FRTC of WECSs.

Author Contributions: Conceptualization, J.C. and B.Y.; validation, J.C. and B.Y.; investigation, J.C. and W.D.; methodology, T.Y. and N.A.; writing—original draft preparation, J.C.; writing—review and editing, W.D. and X.Y.; visualization, H.S. and L.Z.; supervision, H.S. and Y.S.; project administration, J.C., T.Y. and B.Y.; funding acquisition, J.C., T.Y. and B.Y.

Funding: This research was funded by the Natural Science Foundation of the Jiangsu Higher Education Institutions of China (Grant No. 19KJB470036), National Natural Science Foundation of China grant number (Grant Nos. 51667010, 51777078), the Fundamental Research Funds for the Central Universities (Grant No. D2172920), the Key Projects of Basic Research and Applied Basic Research in Universities of Guangdong Province (Grant No. 2018KZDXM001), and the Science and Technology Projects of China Southern Power Grid (Grant No. GDKJXM20172831).

Conflicts of Interest: The authors declare no conflict of interest.

Abbreviations

The following abbreviations are used in this manuscript:

WECSs	Wind energy conversion systems
VSWTs	Variable-speed wind turbines
WT	Wind turbine
DFIGs	Doubly fed induction generators
PMSGs	Permanent magnet synchronous generators
GSC	Grid-side converter
MSC	Machine-side converter
FRTC	Fault ride-through capability
PMSG-WT	Permanent magnet synchronous generator based wind turbine
MPPT	Maximum power point tracking

FLC	Feedback linearisation control
VC	Conventional vector control with proportional-integral
PO-AC	Perturbation observer based adaptive control
LHP	Left-half plane

References

1. Yang, B.; Zhang, X.S.; Yu, T.; Shu, H.C.; Fang, Z.H. Grouped grey wolf optimizer for maximum power point tracking of doubly-fed induction generator based wind turbine. *Energy Convers. Manag.* **2017**, *133*, 427–443. [[CrossRef](#)]
2. Liao, S.W.; Yao, W.; Han, X.N.; Wen, J.Y.; Cheng, S.J. Chronological operation simulation framework for regional power system under high penetration of renewable energy using meteorological data. *Appl. Energy* **2017**, *203*, 816–828. [[CrossRef](#)]
3. Yang, B.; Jiang, L.; Yao, W.; Wu, Q.H. Nonlinear maximum power point tracking control and modal analysis of DFIG based wind turbine. *Int. J. Electr. Power Energy Syst.* **2016**, *74*, 429–436. [[CrossRef](#)]
4. Haque, M.E.; Saw, Y.C.; Chowdhury, M.M. Advanced control scheme for an IPM synchronous generator-based gearless variable speed wind turbine. *IEEE Trans. Sustain. Energy* **2014**, *5*, 354–362. [[CrossRef](#)]
5. Kim, Y.S.; Chung, I.Y.; Moon, S.I. An analysis of variable-speed wind turbine power-control methods with fluctuating wind speed. *Energies* **2013**, *6*, 3323–3338. [[CrossRef](#)]
6. Liu, J.; Yao, W.; Wen, J.Y.; Fang, J.K.; Jiang, L.; He, H.B.; Cheng, S.J. Impact of power grid strength and PLL parameters on stability of grid-connected DFIG wind farm. *IEEE Trans. Sustain. Energy* **2019**. [[CrossRef](#)]
7. Said, B.; Hafedh, A.; Ahmed, E.H.; Mohamed, C. Comparative study of three types of controllers for DFIG in wind energy conversion system. *Prot. Control Mod. Power Syst.* **2018**, *3*, 214–225.
8. Haque, M.E.; Negnevitsky, M.; Muttaqi, K.M. A novel control strategy for a variable-speed wind turbine with a permanent-magnet synchronous generator. *IEEE Trans. Ind. Electron.* **2010**, *46*, 331–339. [[CrossRef](#)]
9. Chinchilla, M.; Arnaltes, S.; Burgos, J.C. Control of permanent-magnet generators applied to variable-speed wind-energy systems connected to the grid. *IEEE Trans. Energy Convers.* **2006**, *21*, 130–135. [[CrossRef](#)]
10. Karakasis, N.E.; Mademlis, C.A. High efficiency control strategy in a wind energy conversion system with doubly fed induction generator. *Renew. Energy* **2018**, *125*, 974–984. [[CrossRef](#)]
11. Yang, B.; Yu, T.; Shu, H.C.; Zhang, Y.M.; Chen, J.; Sang, Y.Y.; Jiang, L. Passivity-based sliding-mode control design for optimal power extraction of a PMSG based variable speed wind turbine. *Renew. Energy* **2018**, *119*, 577–589. [[CrossRef](#)]
12. Liu, J.; Wen, J.Y.; Yao, W.; Long, Y. Solution to short-term frequency response of wind farms by using energy storage systems. *IET Renew. Power Gener.* **2016**, *10*, 669–678. [[CrossRef](#)]
13. Seixas, M.; Relício, R.; Mendes, V.M.F. Fifth harmonic and sag impact on PMSG wind turbines with a balancing new strategy for capacitor voltages. *Energy Convers. Manag.* **2014**, *79*, 721–730. [[CrossRef](#)]
14. Shen, Y.; Yao, W.; Wen, J.Y.; He, H.B.; Jiang, L. Resilient wide-area damping control using GrHDP to tolerate communication failures. *IEEE Trans. Smart Grid* **2019**, *10*, 2547–2557. [[CrossRef](#)]
15. Corradini, M.L.; Ippoliti, G.; Orlando, G. Robust control of variable-speed wind turbines based on an aerodynamic torque observer. *IEEE Trans. Control Syst. Technol.* **2013**, *21*, 1199–1206. [[CrossRef](#)]
16. Hansen, A.D.; Michalke, G. Multi-pole permanent magnet synchronous generator wind turbines' grid support capability in uninterrupted operation during grid faults. *IET Renew. Power Gener.* **2009**, *3*, 333–348. [[CrossRef](#)]
17. Li, S.H.; Haskew, T.A.; Swatloski, R.P.; Gathings, W. Optimal and direct-current vector control of direct-driven PMSG wind turbines. *IEEE Trans. Power Electron.* **2012**, *27*, 2325–2337. [[CrossRef](#)]
18. Hong, C.M.; Chen, C.H.; Tu, C.S. Maximum power point tracking-based control algorithm for PMSG wind generation system without mechanical sensors. *Energy Convers. Manag.* **2013**, *69*, 58–67. [[CrossRef](#)]
19. Xia, Y.; Ahmed, K.H.; Williams, B.W. A new maximum power point tracking technique for permanent magnet synchronous generator based wind energy conversion system. *IEEE Trans. Power Electron.* **2011**, *26*, 3609–3620. [[CrossRef](#)]
20. Li, H.; Shi, K.L.; McLaren, P.G. Neural-network-based sensorless maximum wind energy capture with compensated power coefficient. *IEEE Trans. Ind. Appl.* **2005**, *41*, 1548–1556. [[CrossRef](#)]

21. Abdullah, M.A.; Yatim, A.H.M.; Tan, W.C.; Saidur, R. A review of maximum power point tracking algorithms for wind energy systems. *Renew. Sustain. Energy Rev.* **2012**, *16*, 3320–3327. [[CrossRef](#)]
22. Camblong, H. Digital robust control of a variable speed pitch regulated wind turbine for above rated wind speeds. *Control Eng. Pract.* **2008**, *16*, 946–958. [[CrossRef](#)]
23. Kumar, A.; Stol, K. Simulating feedback linearization control of wind turbines using high-order models. *Wind Energy* **2009**, *13*, 419–432. [[CrossRef](#)]
24. Boukhezzar, B.; Siguerdidjane, H. Nonlinear Control of a variable-speed wind turbine using a two-mass model. *IEEE Trans. Energy Convers.* **2011**, *26*, 149–162. [[CrossRef](#)]
25. Tsili, M.; Papathanassiou, S. A review of grid code technical requirements for wind farms. *IET Renew. Power Gener.* **2009**, *3*, 308–332. [[CrossRef](#)]
26. Lee, C.T.; Hsu, C.W.; Cheng, P.T. A low-voltage ride-through technique of grid-connected converters of distributed energy resources. *IEEE Trans. Ind. Appl.* **2011**, *47*, 1812–1832. [[CrossRef](#)]
27. Kim, K.H.; Jeung, Y.C.; Lee, D.C.; Kim, H.G. LVRT scheme of PMSG wind power systems based on feedback linearization. *IEEE Trans. Power Electron.* **2012**, *27*, 2376–2384. [[CrossRef](#)]
28. Popat, M.; Wu, B.; Zargari, N.R.; Fault ride-through capability of cascaded current-source converter-based offshore wind farm. *IEEE Trans. Sustain. Energy* **2013**, *4*, 314–323. [[CrossRef](#)]
29. Iov, F.; Hansen, A.; Sorensen, P.; Cutululis, N. *Mapping of Grid Faults and Grid Codes*; Risoe National Laboratory, Technical University of Denmark: Copenhagen, Denmark, 2007.
30. Yang, J.; Gao, Y.J.; O'Reilly, J. Permanent magnet synchronous generator converter protection analysis during DC wind farm open-circuit fault condition. In Proceedings of the 2009 IEEE Electrical Power & Energy Conference (EPEC), Montreal, QC, Canada, 22–23 October 2009; pp. 1–6.
31. Noureldeen, O.; Hamdan, I. A novel controllable crowbar based on fault type protection technique for DFIG wind energy conversion system using adaptive neuro-fuzzy inference system. *Prot. Control Mod. Power Syst.* **2018**, *3*, 328–339. [[CrossRef](#)]
32. Rizo, M.; Rodriguez, A.; Bueno, E.; Rodriguez, F.J.; Giron, C. Low voltage ride-through of wind turbine based on interior permanent magnet synchronous generators sensorless vector controlled. In Proceedings of the 2010 IEEE Energy Conversion Congress and Exposition, Atlanta, GA, USA, 12–16 September 2010; pp. 2507–2515.
33. Seman, S.; Niiranen, J.; Arkkio, A. Ride-through analysis of doubly fed induction wind-power generator under unsymmetrical network disturbance. *IEEE Trans. Power Syst.* **2006**, *21*, 1782–1789. [[CrossRef](#)]
34. Dai, J.Y.; Xu, D.W.; Wu, B.; Zargari, N.R. Unified DC-Link current control for low-voltage ride-through in current-source-converter-based wind energy conversion systems. *IEEE Trans. Power Electron.* **2011**, *26*, 288–297.
35. Liang, J.Q.; Qiao, W.; Harley, R.G. Direct transient control of wind turbine driven DFIG for low voltage ride-through. In Proceedings of the 2009 IEEE Power Electronics and Machines in Wind Applications, Lincoln, NE, USA, 24–26 June 2009; pp. 1–7.
36. Grilo, A.P.; Mota, A.S.A.; Mota, L.T.M.; Freitas, W. An analytical method for analysis of large-disturbance stability of induction generators. *IEEE Trans. Power Syst.* **2007**, *22*, 1861–1869. [[CrossRef](#)]
37. Vrionis, T.; Koutiva, X.; Vovos, N.; Giannakopoulos, G. Control of an HVDC link connecting a wind farm to the grid for fault ride-through enhancement. *IEEE Trans. Power Syst.* **2007**, *22*, 2039–2047. [[CrossRef](#)]
38. Conroy, J. F.; Watson, R. Low voltage ride-through of a full converter wind turbine with permanent magnet generator. *IET Renew. Power Gener.* **2007**, *1*, 182–189. [[CrossRef](#)]
39. Mullane, A.; Lightbody, G.; Yacamini, R. Wind turbine fault ride through enhancement. *IEEE Trans. Power Syst.* **2005**, *20*, 1929–1937. [[CrossRef](#)]
40. Matas, J.; Castilla, M.; Guerrero, J.M.; Garcia de Vicuna, L.; Miret, J. Feedback linearization of direct-drive synchronous wind turbines via a sliding mode approach. *IEEE Trans. Power Electron.* **2008**, *23*, 1093–1103. [[CrossRef](#)]
41. Matas, J.; Rodriguez, P.; Guerrero, J.M.; Vasquez, J.C. Ride through improvement of wind-turbines via feedback linearization. In Proceedings of the 2008 IEEE International Symposium on Industrial Electronics, Cambridge, UK, 30 June–2 July 2008; pp. 2377–2382.
42. Valenciaga, F.; Puleston, P.F.; Battaiotto, P.E. Variable structure system control design method based on a differential geometric approach to a wind energy conversion subsystem. *IEE Proc.-Control Theory Appl.* **2004**, *151*, 6–12. [[CrossRef](#)]

43. Hosseinzadeh, M.; Rajaei Salmasi, F. Analysis and detection of a wind system failure in a micro-grid. *J. Renew. Sustain. Energy* **2016**, *8*, 043302. [[CrossRef](#)]
44. Hosseinzadeh M.; Yazdanpanah, M.J. Performance enhanced model reference adaptive control through switching non-quadratic Lyapunov functions. *Syst. Control Lett. Syst.* **2015**, *76*, 47–55. [[CrossRef](#)]
45. Chen, J.; Jiang, L.; Yao, W.; Wu, Q.H. Perturbation estimation based nonlinear adaptive control of a full-rated converter wind-turbine for fault ride-through capability enhancement. *IEEE Trans. Power Syst.* **2014**, *29*, 2733–2743. [[CrossRef](#)]
46. Yang, B.; Yu, T.; Shu, H.C.; Dong, J.; Jiang, L. Robust sliding-mode control of wind energy conversion systems for optimal power extraction via nonlinear perturbation observers. *Appl. Energy* **2018**, *210*, 711–723. [[CrossRef](#)]
47. Chen, J.; Yao, W.; Zhang, C.K.; Ren, Y.X.; Jiang, L. Design of robust MPPT controller for grid-connected PMSG-Based wind turbine via perturbation observation based nonlinear adaptive control. *Renew. Energy* **2019**, *134*, 478–495. [[CrossRef](#)]
48. Uehara, A.; Pratap, A.; Goya, T.; Senjyu, T.; Yona, A.; Urasaki, N.; Funabashi, T. A coordinated control method to smooth wind power fluctuations of a PMSG-based WECS. *IEEE Trans. Energy Convers.* **2011**, *26*, 550–558. [[CrossRef](#)]
49. Jiang, L.; Wu, Q.H.; Wen, J.Y. Decentralized nonlinear adaptive control for multimachine power systems via high-gain perturbation observer. *IEEE Trans. Circuits Syst. I Regul. Pap.* **2004**, *51*, 2052–2059. [[CrossRef](#)]
50. Jiang, L.; Wu, Q.H. Nonlinear adaptive control via sliding-mode state and perturbation observer. *IEE Proc. Inst. Electr. Eng.-Control Theory Appl.* **2002**, *149*, 269–277. [[CrossRef](#)]
51. Tao, G. Model reference adaptive control with $L^{1+\alpha}$ tracking. *Int. J. Control.* **1996**, *64*, 859–870. [[CrossRef](#)]
52. Alepuz, S.; Calle, A.; Busquets-Monge, S.; Kouro, S.; Wu, B. Use of stored energy in PMSG rotor inertia for low-voltage ride-through in back-to-back NPC converter-based wind power systems. *IEEE Trans. Ind. Electron.* **2013**, *60*, 1787–1796. [[CrossRef](#)]
53. Heier, S. *Grid Integration of Wind Energy Conversion Systems*; Wiley: Hoboken, NJ, USA, 2006.



© 2019 by the authors. Licensee MDPI, Basel, Switzerland. This article is an open access article distributed under the terms and conditions of the Creative Commons Attribution (CC BY) license (<http://creativecommons.org/licenses/by/4.0/>).